IEEE Access
Multidisciplinary | Rapid Review | Open Access Journal

Received October 19, 2021, accepted November 21, 2021, date of publication November 23, 2021,
date of current version December 8, 2021.

Digital Object Identifier 10.1109/ACCESS.2021.3130425

A Metasurface-Based Single-Layered Compact AMC-Backed Dual-Band Antenna for Off-Body IoT Devices

SAROSH AHMAD[1,2], (Student Member, IEEE), KASHIF NISAR PARACHA[2], (Senior Member, IEEE), YAWAR ALI SHEIKH[2], ADNAN GHAFFAR[3], ARSLAN DAWOOD BUTT[2], MOHAMMAD ALIBAKHSHIKENARI[1], (Member, IEEE), PING JACK SOH[4,5], (Senior Member, IEEE), SALAHUDDIN KHAN[6], AND FRANCISCO FALCONE[7,8], (Senior Member, IEEE)

[1]Department of Signal Theory and Communications, Universidad Carlos III de Madrid, Leganés, 28911 Madrid, Spain
[2]Department of Electrical Engineering and Technology, Government College University Faisalabad (GCUF), Faisalabad 38000, Pakistan
[3]Department Electrical and Electronic Engineering, Auckland University of Technology, Auckland 1010, New Zealand
[4]Advanced Communication Engineering (ACE) CoE, Faculty of Electronic Engineering Technology, Universiti Malaysia Perlis, Perlis 01000, Malaysia
[5]Centre for Wireless Communications (CWC), University of Oulu, 90014 Oulu, Finland
[6]Department of Electrical Engineering, College of Engineering, King Saud University, Riyadh 11451, Saudi Arabia
[7]Electric, Electronic and Communication Engineering Department, Public University of Navarre, 31006 Pamplona, Spain
[8]Institute of Smart Cities, Public University of Navarre, 31006 Pamplona, Spain

Corresponding authors: Sarosh Ahmad (saroshahmad@ieee.org), Mohammad Alibakhshikenari (mohammad.alibakhshikenari@uc3m.es), and Francisco Falcone (francisco.falcone@unavarra.es)

This work was supported in part by the Universidad Carlos III de Madrid; in part by the European Union's Horizon 2020 Research and Innovation Programme under Marie Sklodowska-Curie Grant 801538; in part by the Ministerio de Ciencia, Innovación y Universidades, Gobierno de España (MCIU/AEI/FEDER and UE) under Grant RTI2018-095499-B-C31; and in part by the Researchers Supporting Project, King Saud University, Riyadh, Saudi Arabia, under Project number RSP-2021/58.

ABSTRACT In this article, a compact printed monopole dual-band antenna using artificial magnetic conductor (AMC)-plane with improved gain and broader bandwidth, applicable for off-body internet of things (IoT) devices is presented. The monopole antenna consists of two C-shaped resonators connected through a U-shaped monopole, parasitic elements, discrete ground circular rings and a co-planar waveguide (CPW) feedline. Each artificial magnetic conductor (AMC) unit cell consists of a slotted circular and a square stubs, designed with two zero-crossing phases for improving the radiation characteristics and to achieve the high gain. The overall size of the proposed AMC-backed antenna is 44.4 mm × 44.4 mm × 1.6 mm with electrical dimensions of $0.75\lambda_g \times 0.75\lambda_g \times 0.027\lambda_g$. This AMC-backed antenna featured measured bandwidths of 9.6% and 12.4% with improved measured gain values of 4.88 dB and 4.73 dB at 2.45 GHz and 5.8 GHz, respectively. The specific absorption rate (SAR) values are analysed and found to be 1.58 W/kg at 2.45 GHz and 0.9 W/kg at 5.8 GHz. Therefore, the proposed AMC-backed antenna is useful for off-body IoT devices operating at 2.45 and 5.8 GHz industrial, scientific, and medical (ISM) band applications.

INDEX TERMS Antennas, metasurfaces, artificial magnetic conductors, wireless body area network, specific absorption rate, Internet of Things.

I. INTRODUCTION

The main objective of a Wireless Body Area Networks (WBANs) is to provide a consistent interconnection between various body-centric devices for communication and sensing. An example of its application in remote patient health monitoring system is presented in **Figure 1**. These devices can either be used for (in, on, or off)-body communication devices. In off-body communication, networking among body-worn devices and their surroundings is established for effective transmission/reception. Antenna structures for the off-body application typically must be compatible with clothing with consistent performance under bending and human proximity effects and comply to specific absorption rate (SAR) restrictions [1]–[4]. Since the antenna is utilized for off-body IoT devices therefore it is necessary to discuss its application in brief details [5]. The antenna can be utilized for many off-body IoT devices like smart hand watch wearable

The associate editor coordinating the review of this manuscript and approving it for publication was Santi C. Pavone.

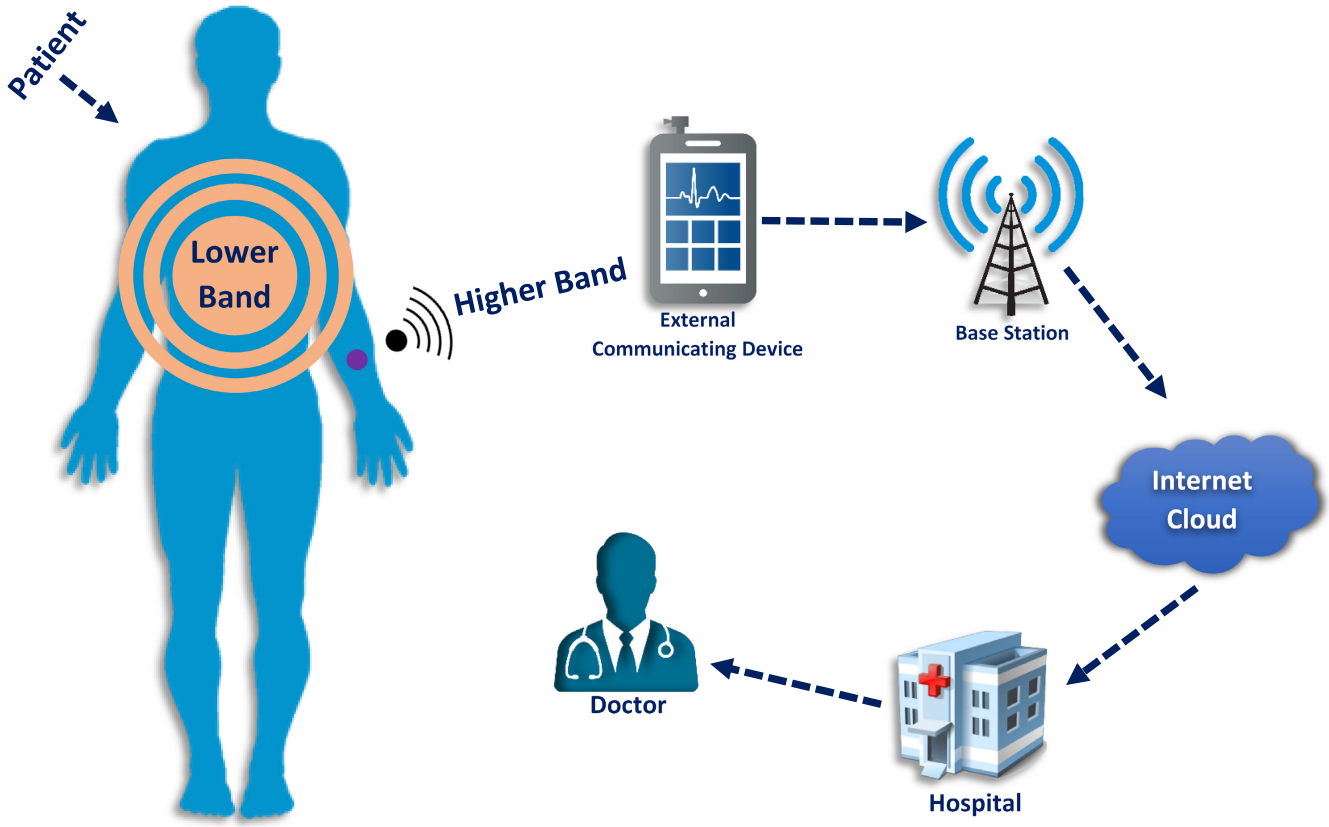

FIGURE 1. Schematic diagram of off-body antenna for wireless communication.

applications, patient to doctor communications, and man to vehicle communications etc. The antenna integrated on an IoT device will exhibit a directional radiation pattern in order to send the information of the patient to the doctor's gadget [6]. Since the directional radiation pattern is an important feature of off-body antennas, therefore it is proposed that the antenna is suitable for off-body IoT devices [7]–[10].

A compact size low-profile antenna comprising of an L-shape slotted patch for biomedical and internet of things (IoT) was reported in [9]. The simple microstrip patch antenna for the applications in WBAN was explained in [11]. The antenna was a single band operated at 2.45 GHz. The antenna consisted of three metallic fabric layers of substrate separated by the fourth layer of felt substrate. The complete volume of the antenna reported is $80 \times 80 \times 8.6$ mm^3($0.71\lambda_g \times 0.71\lambda_g \times 0.076\lambda_g$). The antenna covered the bandwidth 2.4-2.52 GHz (4.9%) at 2.45 GHz. A microstrip simple patch antenna for wearable applications operated in ISM band was presented in [12]. The total area of the patch antenna was found to be 60×60 mm^2 ($0.73\lambda_g \times 0.73\lambda_g$) The reported frequency range of the antenna was 2.4-2.5 GHz (4.1%) at 2.45 GHz. The oval-shaped radiating patch antenna was presented in [13]. It was comprised of an extended CPW semi-circular ground plane based on electromagnetic bandgap (EBG) resonating at 2.45 GHz for WBAN applications. The overall volume of the design with EBG was $75.7 \times 75.7 \times 0.1$ mm^3($1.05\lambda_g \times 1.05\lambda_g \times 0.0014\lambda_g$) with a bandwidth from 2.4 to 2.56 GHz (6.53%). Despite the satisfactory performance, its size was relatively large. Another EBG-based single band antenna with discrete ground structure was proposed for medical wearable applications [14]. The patch antenna consisted of an E-shaped radiator with half ground plane to operate at 2.4 GHz with a bandwidth of about 32.08% and a size of $60 \times 60 \times 2.4$ mm^3 ($0.64\lambda_g \times 0.64\lambda_g \times 0.026\lambda_g$) on a fabric substrate.

A low-profile dual-layered substrate antenna operating in dual-frequency mode was designed [8]. Both substrate layers are made up of FR-4 (lossy), each with 0.6 mm thickness. The radiating patch contained a thin copper line with two arms and two rectangular patches. Both arms were connected with the second layer of the substrate's ground via two shorting pins. The $50 \times 50 \times 0.6$ mm^3 ($0.856\lambda_g \times 0.856\lambda_g \times 0.01\lambda_g$) sized antenna operated with bandwidths of about 4.2% at 2.45 GHz and 10.2% at 5.8 GHz. The antenna featured a peak gain of 1.2 dB at 2.45 GHz, and 7.9 dB at 5.8 GHz. The spherical patch antenna was designed to implemented on a FR-4 substrate (1.57 mm-thick) for on-, and off-body links [15]. The radiating patch consisted of two circular shape radiators connected to the feedline with the help of a shorting pin. It was worked at 1.9 GHz and 2.45 GHz, with a size of $60 \times 60 \times 1.57$ mm^3 ($1.03\lambda_g \times 1.03\lambda_g \times 0.027\lambda_g$)

which was relatively large. A double-resonance antenna for on-, and off-body body communication was presented in [7]. The proposed antenna has volume of 30 × 45 × 3.2 mm^3 (0.514λ_g × 0.77λ_g × 0.054λ_g). The antenna consisted of two FR-4 layers and operated at 2.4 GHz and 5.8 GHz frequency bands. The antenna reported a bandwidth of 4.9% at 2.4 GHz and 2.8% at 5.8 GHz, respectively. The realized gain of the antenna was 0.56 dBi at 2.4 GHz and -1.59 dBi at 5.8 GHz. A split-ring resonator (SRR)-shaped bar-slotted textile antenna resonating at 2.45 GHz and 3.5 GHz with operating bandwidths of about 5.3% and 3.14% was proposed in [16]. The antenna had overall dimensions of about 70 × 70 × 3 mm^3(0.69λ_g × 0.69λ_g × 0.029λ_g), which has large size with narrow bandwidths. The wearable patch antenna of size 80 mm × 92 mm (0.75λ_g × 0.86λ_g) for medical applications was proposed in [17] on a felt substrate of 2 mm-thickness. The operating range of this antenna was from 1.7 to 2.5 GHz centered at 2 GHz, and from 5.4 to 5.95 GHz centered at 5.8 GHz.

In another study, a dual-band circular patch antenna printed on the F4B substrate with a thickness of 3.2 mm was presented in [18]. The operating bandwidth of the antenna was 2.57% at lower band and 5.22% at upper band. The overall size of the antenna was 100 × 100 × 3.2 mm^3 (1.33λ_g × 1.33λ_g × 0.042λ_g). In [19], a dual-band circular patch textile-based antenna with the size of 100 × 100 mm^2 (0.9λ_g × 0.9λ_g) for on-, and off-body links was explained. The circular patch had eight slots on its edge. The reported antenna resonated at 2.45 GHz and 5.8 GHz from 2.398 to 2.517 GHz (4.9%) at 2.45 GHz and from 5.697 to 5.915 GHz (3.8%) at 5.8 GHz.

A diamond-shaped dual-band AMC-backed patch antenna printed on Roger 3003C for indoor and outdoor wearable applications was proposed in [20], This antenna resonated at 1.575 GHz and 2.45 GHz with 1.84% and 0.736% of bandwidths, respectively. The thickness of the semi-flexible substrate was 3.04 mm, with an overall antenna size of 130.8 × 130.8 mm^2 (1.85λ_g × 1.85λ_g). The proposed antenna had comparatively large size with narrow impedance bandwidths. Another AMC-backed dual-band antenna working at 0.86 GHz and 2.4 GHz for wearable applications was reported in [21]. This meandered shaped antenna was fully rolled onto a watch strap and was simulated on a human arm phantom (skin, fat, and muscle) but the antenna did not show a good performance on human arm model. However, the area of the reported antenna was 195 × 30 mm^2 (1.67λ_g × 0.4λ_g) and its SAR values were not calculated. An AMC-backed antenna for health monitoring applications was fabricated on a polyimide substrate of 0.15 mm-thickness in [22]. It had size of 59.1 mm × 59.1 mm (0.9λ_g × 0.9λ_g) with operational bandwidths of 4.08% at 2.45 GHz and 2.24% at 5.8 GHz. The proposed antenna showed wide bandwidth but the antenna size was relatively large.

This paper describes a compact metamaterial-based dual-band monopole antenna for off-body communication, sized at 44.4 × 44.4 × 1.6 mm^3 (0.75λ_g × 0.75λ_g × 0.027λ_g).

TABLE 1. Optimized parameters of the proposed design.

Dimensions	Values (mm)	Dimensions	Values (mm)
Ls	30	*Ws*	14
Le	13	*We*	4.0
Lf	15.5	*Wf*	1.0
Lg	2.5	*Wg*	6.35
L1	8.8	*w1*	4.50
L2	0.80	*w2*	3.25
L3	6.8	*w3*	1.25
L4	4.0	*w4*	3.75
L5	4.0	*w5*	1.70
R1	3.0	*g*	0.15
R2	4.5	*g1*	2.50
R_L	10.8	h_{sub}	1.60

To achieve high gain and larger bandwidth with compact size is not simple and has become the main focus of the researchers, now-a-days. Therefore, a co-planar waveguide (CPW) technique with defected ground circular rings and parasitic elements on both sides of the top layer of the substrate are utilized to keep the antenna's size as compact as possible. Parasitic elements help to tune the lower frequency band (2.45 GHz) while discrete ground circular rings tune the upper frequency band at 5.8 GHz. To make the antenna biocompatible to human body and to achieve directional radiation pattern, a novel miniaturized dual band AMC-unit cell of size 14.8 × 14.8 × 1.6 mm^3(0.25λ_g × 0.25λ_g × 0.027λ_g) is created. With AMC-plane of 3 × 3 array, the antenna has achieved broadsided directional radiation pattern, higher bandwidth, high gain, and reduced SAR values. In this paper, the antenna design procedure is explained in Section II, followed by the AMC unit cell design in Section III. The performance of the antenna with AMC-backing in free space and in proximity of human body is illustrated in Section IV and V, correspondingly. Finally, our concluding remarks are discussed in Section VI.

II. ANTENNA DESIGN

A. DESIGN PROCEDURE OF THE DUAL-BAND ANTENNA

A simple dual-band monopole antenna with two C-shaped resonators connected with a U-shaped patch is proposed, fed by a co-planar waveguide (CPW) technique. The presented antenna contains three distinct layers: a ground plane, a low-cost 1.6 mm-thick FR-4 substrate (ε_r = 4.3 and $tan\delta$ = 0.025) and a radiating patch (from bottom to top), as shown in **Figure 2**. The parasitic elements and the discrete ground circular rings are introduced to set the frequency at the required bands i.e., 2.45 GHz and 5.8 GHz keeping the overall size of the antenna compact. The complete volume of the antenna is 30 × 14 × 1.6 mm^3. The optimized values of this antenna are summarized in **Table 1**.

The design procedure of the dual-band antenna is explained as follows: The basic antenna design (ANT I in Figure 3(a)) consists of a 50-Ω CPW feedline, discrete ground circular rings, and a rectangular patch. The patch's width and length

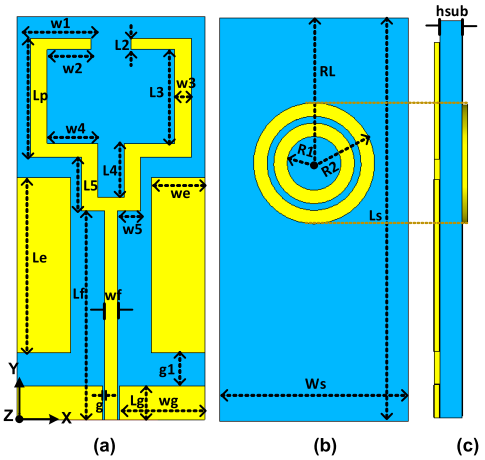

FIGURE 2. Proposed antenna's structure, a) front view, b) back view, (c) side view.

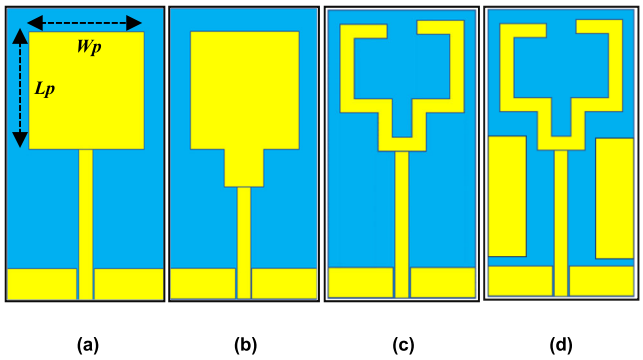

FIGURE 3. Radiating patch design steps; (a) rectangular patch (ANT I), (b) modified patch (ANT II), (c) two monopoles (ANT III), (d) Two monopoles with parasitic elements (ANT IV).

are calculated using (1) and (2) [18], as follows:

$$Wp = \frac{\lambda_o}{2(\sqrt{0.5(\varepsilon_r + 1)}} \tag{1}$$

and

$$Lp = \frac{c_o}{2f_o\sqrt{\varepsilon_{eff}}} - 2\Delta L_p \tag{2}$$

Using $\varepsilon_r = 4.3$, $h_{\text{sub}} = 1.6$ mm, the initial dimensions of the rectangular patch are $L_p = 8.8$ mm and $W_p = 9.8$ mm. Upon full wave optimization, the width and length of the patch are $L_p = 8.8$ mm and $W_p = 9.8$ mm.

The design steps for the presented antenna are shown in **Figure 3**. ANT I is the basic rectangular patch with -10 dB reflection coefficient but in this instance, the antenna is resonating only at 2.6 GHz and 6.8 GHz frequencies. *'Lp'* and *'Wp'* are the radiating patch's length and width (8.8×9.8 mm^2). Then, to shift the frequency towards the lower band, another small patch is created at the bottom side of the first rectangular patch, as illustrated in ANT II (Figure 3(b)). This shifts the resonating frequency to the lower frequency band and keep its S_{11} value below -10 dB at 2.55 GHz and 6.2 GHz. Now in the third case (ANT III), the rectangular patch is truncated to create two monopoles. This results in an operation at 2.5 GHz and 5.82 GHz. In order to

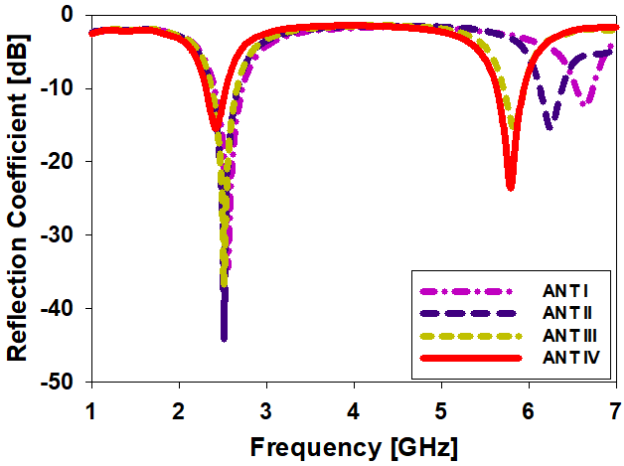

FIGURE 4. Simulation results comparison of S_{11} for the design steps shown in Fig. 3.

move the lower band towards 2.45 GHz while keeping the size compact, the discrete ground circular rings are added behind the substrate and the parasitic elements are introduced on the left and right side of the substrate just below the radiators as presented in ANT IV. Simulation results of all design steps are compared in **Figure 4** indicating the ease of impedance tuning in the upper and lower bands using the parasitic elements and the discrete ground circular rings.

B. PARAMETRIC ANALYSIS OF THE DUAL-BAND ANTENNA

The analysis of the parameters of the dual-band antenna is fully explained in this section. The reflection coefficient in the lower and upper bands can be adjusted by varying the values of the pole's length *'L3'*, width of the poles *'W3'* and length of the pole *'W2'* as presented in **Figure 5**. Figure 5 (a) illustrates that by changing the value of *'L3'* from 3.8 mm to 6.8 mm, the upper frequency band shifted from 4.75 GHz to 5.8 GHz (1.05 GHz), and the lower band varied from 1.3 GHz to 2.45 GHz (1.15 GHz). When the value of the *'W3'* is changed from 0.5 mm to 2.5 mm then the upper frequency band shifted from 5.25 GHz to 6.15 GHz (900 MHz) while the lower band changed from 2 GHz to 2.9 GHz (900 MHz) as presented in Figure 5(b). From Figure 5(c), it is also noticed that when the values of the *'W2'* varied from 1.25 mm to 5.25 mm then the upper band shifted from 5.3 GHz to 6.1 GHz (800 MHz) and the lower band moved from 2 GHz to 2.95 GHz (950 MHz). Now again, in order to highlight the presence of the parasitic elements and the discrete ground circular rings it is necessary to do optimization of its parameters. So, there is a change in the upper frequency band if the position of the discrete ground circular rings *'RL'* are varied. By decreasing the values of the *'RL'* from 11 mm to 5.5 mm, the upper band moved from 5.2 GHz to 5.8 GHz (600 MHz) with minimum return loss while in the case of lower band, it is varied from 1.9 GHz to 2.9 GHz (1 GHz) as described in Figure 5(d). Now, by varying the length of the parasitic elements *'Le'* from 10 mm to 15 mm, the lower frequency band shifted

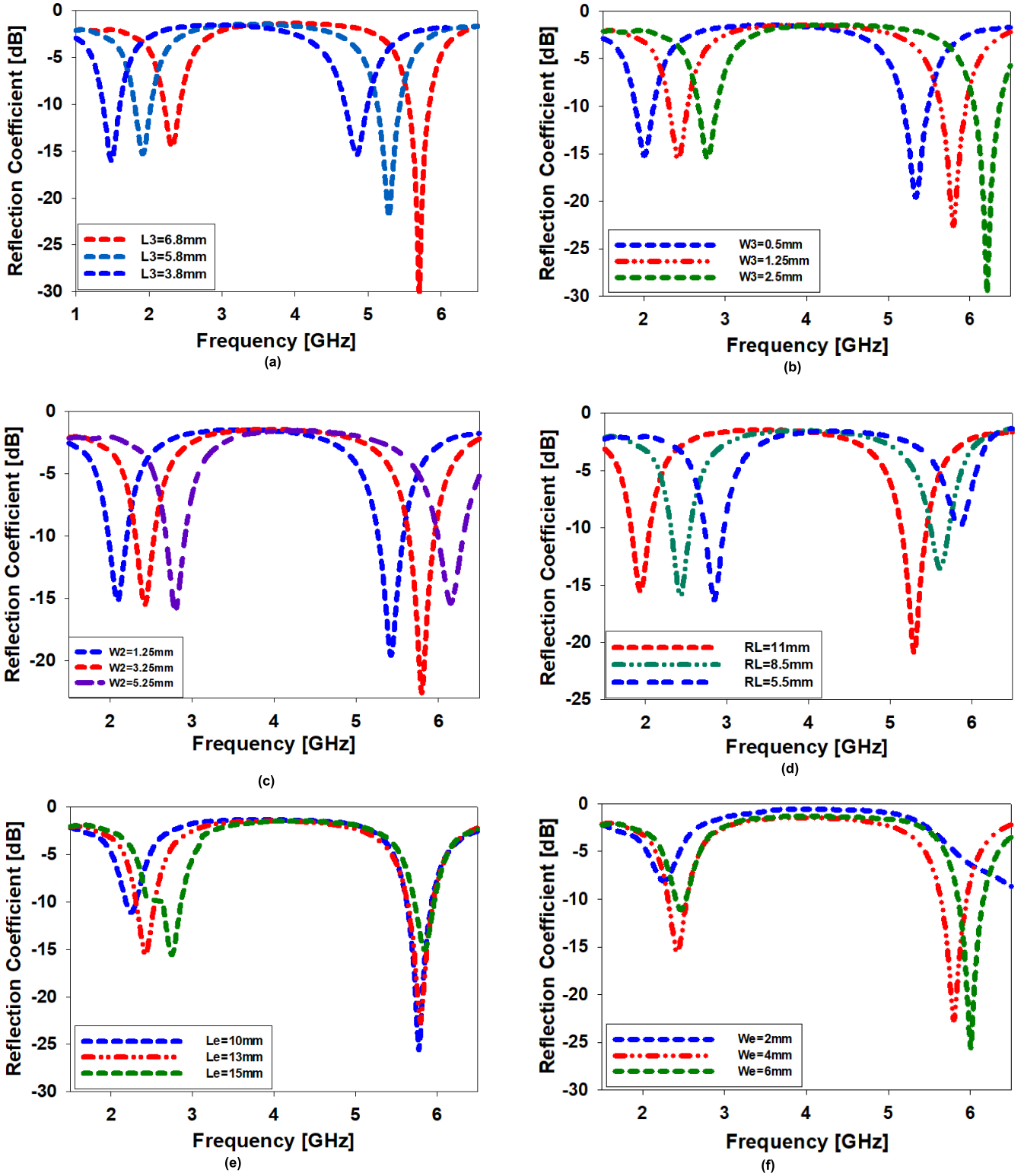

FIGURE 5. Parametric study of the antenna; (a) variation in '*L3*', (b) variation in '*W3*', (c) variation in '*W2*', (d) variation in '*RL*', (e) variation in '*Le*', (f) variation in '*We*'.

from 2.2 GHz to 2.7 GHz (500 MHz) while the upper band changed a bit as presented in Figure 5 (e). When the width of the parasitic elements '*We*' are varied from 2 mm to 6 mm then the upper frequency band displaced from 5.8 GHz and shifted to the higher frequency bands as shown in Figure 5(f).

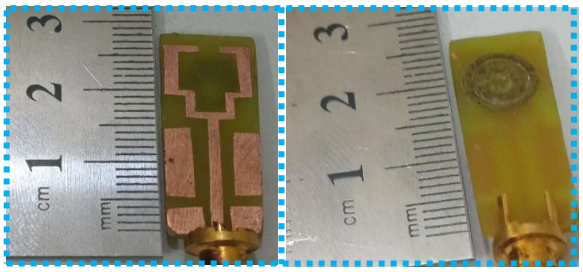

FIGURE 6. Prototype fabricated antenna; (a) front view, (b) back view.

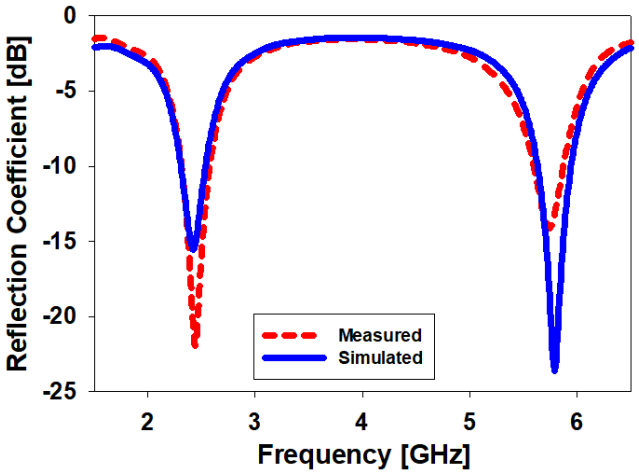

FIGURE 7. Measured reflection coefficient of the prototype fabricated antenna.

C. FABRICATED PROTOTYPE OF THE PROPOSED ANTENNA

The proposed dual-band radiating patch is fabricated on a low-cost FR-4 (lossy) substrate, the front view and the back view of the fabricated model are presented in **Figure 6**. In the case of simulations results, the presented antenna covers the bandwidths 2.30-2.53 (230 MHz) at 2.45 GHz and 5.62-5.92 (300 MHz) at 5.8 GHz, while in the case of measurement results, the antenna covers the bandwidths 2.30-2.54 GHz (240 MHz) at 2.45 GHz and 5.63-5.95 GHz (320 MHz) at 5.8 GHz as illustrated in **Figure 7**.

Figure 8 illustrates the simulation results of the radiation pattern along *xz*- and *yz*-planes in free space. The two-dimensional (2D) far-field describes the behavior of the antenna. The proposed antenna behaves as spherical shaped pattern in both planes at 2.45 GHz, and the antenna behaves as omnidirectional radiation pattern in both planes at 5.8 GHz. The peak gain of the antenna is calculated as 0.574 dB (at 2.45 GHz) and 3.84 dB (at 5.8 GHz).

The current density of the dual-band antenna is presented in **Figure 9**. Since, the current density helps to find out the resonating elements inside the patch antenna and tells the direction of the current flow. At the lower band (at 2.45 GHz), the current mostly flows around the U-shaped patch, CPW-feedline, and some number of current flows through the parasitic elements and the discrete ground

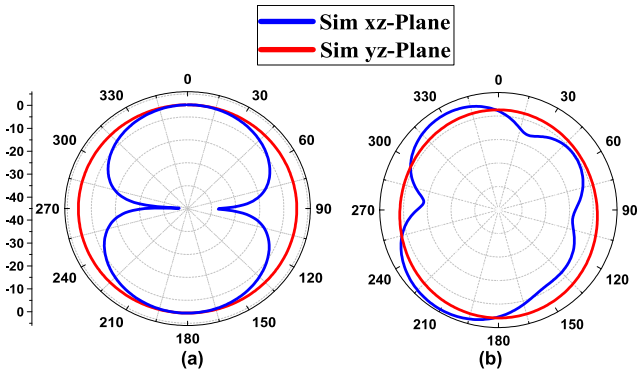

FIGURE 8. 2D radiation pattern in free space; (a) at 2.45GHz, (b) at 5.8GHz.

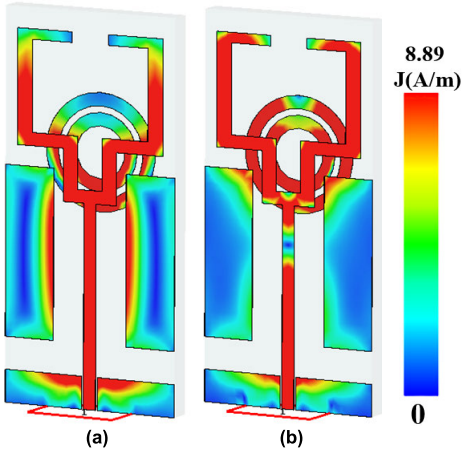

FIGURE 9. Current distribution throughout the patch; (a) at 2.45GHz, (b) at 5.8GHz.

circular rings, while in the case of upper frequency band (at 5.8 GHz), the surface current circulates in C-shaped resonators and most of the current flow through the discrete ground circular rings that have proved the highest surface current at 5.8 GHz.

D. EQUIVALENT CIRCUIT MODEL FOR THE DUAL-BAND ANTENNA

An advanced design system (ADS) software is used to design the proposed circuit model as demonstrated in [23] **Figure 10** and its simulation results are also presented in Figure 11. The proposed model contains two parallel RLC (resistor-inductor-capacitor) circuits coupled in series with one inductor and one capacitor to model the antenna input impedance and the operation in the two bands. The values of inductors, resistors, and capacitors are summarized in **Table 2**.

To obtain operation in the lower band i.e., 2.45 GHz, two capacitors are connected in parallel with two inductors and one resistor. In the same way, another parallel RLC circuit is designed to achieve the upper-frequency band i.e., 5.8 GHz. In this case, a capacitor is connected in parallel with an inductor and a resistor. The S_{11} of the circuit model can be improved by adjusting the values of the resistors. The comparison among the simulation results of the circuit model

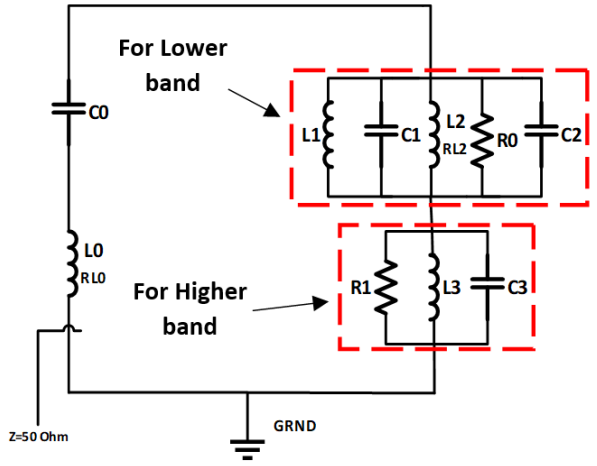

FIGURE 10. Proposed circuit model for the dual-band antenna.

TABLE 2. List of the values for the equivalent circuit model.

Inductors	Values (nH)	Capacitors	Values (pF)	Resistors	Values (Ω)
L0	5×10^{-3}	C0	2.2	R0	50
L1	1.0	C1	2.2	R1	50
L2	8.0	C2	2	R_{L0}	5
L3	38.9×10^{-3}	C3	19	R_{L2}	25

and the full-wave optimization of the presented antenna are presented in **Figure 11**.

E. PARAMETRIC ANALYSIS OF THE EQUIVALENT CIRCUIT MODEL FOR THE DUAL-BAND ANTENNA

To change the operation in the lower band, the values of *'L1'*, *'C1'*, *'L2'*, and *'C2'* can be varied, as presented in **Figure 12** (a). For instance, the lower band can be moved from 2.45 GHz to 2.3 GHz by increasing the value of *'C1'* from 2.2 pF to 3 pF and *'C2'* from 2 pF to 3 pF. Meanwhile, by decreasing the value of *'L2'* from 8 nH to 2 nH, the lower frequency band shifts from 2.45 GHz to 1.8 GHz (650 MHz) and by increasing the value of *'L1'* from 1 nH to 2 nH it moves from 2.45 GHz to 2.75 GHz (300 MHz). For the upper band, two values of *'C3'* and *'L3'* can be varied, as shown in Figure 12(b). By increasing the value of *'C3'* from 19 pF to 22 pF, the upper band shifts from 5.8 GHz to 5.6 GHz (200 MHz), and by decreasing the value of *'C3'* from 19 pF to 18 pF, the upper band shifts from 5.8 GHz to 6 GHz (200 MHz). Similarly, by increasing the value of *'L3'* from 38.9 pH to 45 pH, the upper band moves from 5.8 GHz to 5.6 GHz (200 MHz), and by decreasing the value of *'L3'* from 38.9 pH to 25 pH, frequency shifts from 5.8 GHz to 6.1 GHz (300 MHz).

III. AMC UNIT CELL DESIGN

A. DESIGN PROCEDURE OF THE UNIT CELL

Artificial magnetic conductor (AMC) can be used to control the propagation of electromagnetic waves, which makes them suitable to improve the gain and to ensure the directional radiation pattern [24]. A simple and miniaturized AMC unit cell is printed on an FR-4 substrate (h_{sub} = 1.6mm and

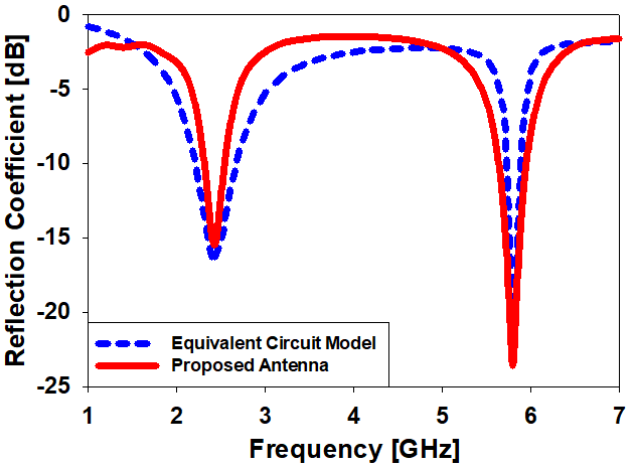

FIGURE 11. Reflection coefficient [dB] comparison between the equivalent circuit model and the proposed antenna.

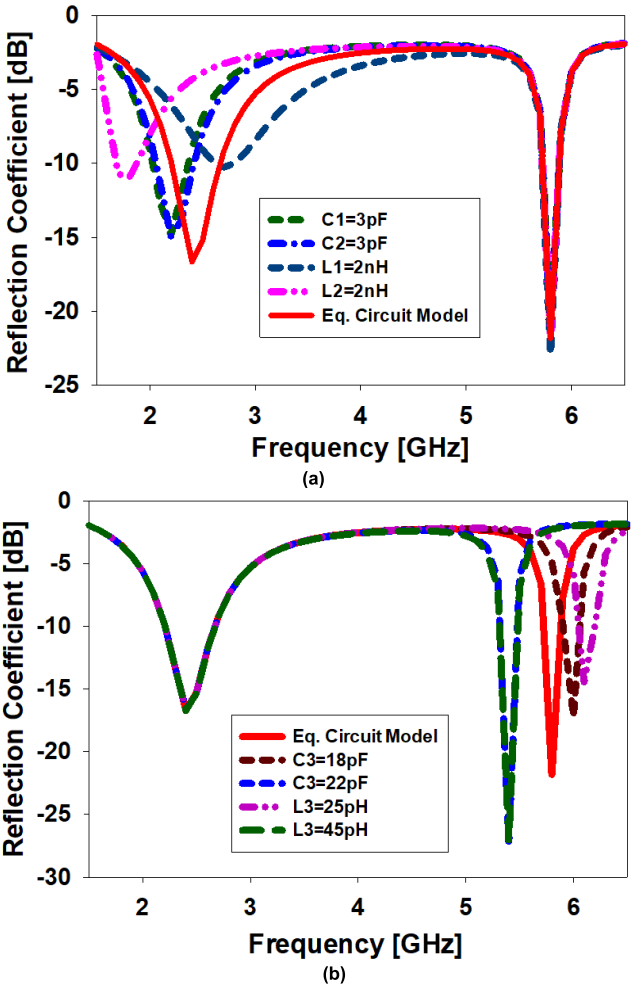

FIGURE 12. Parametric optimization of the equivalent circuit model for the dual-band antenna; (a) for the lower band (2.45 GHz), (b) for the upper band (5.8 GHz).

$tan\delta$ = 0.025) in this work. Its overall size is 14.8 × 14.8 × 1.6 mm^3($0.25\lambda_g \times 0.25\lambda_g \times 0.027\lambda_g$), as presented in **Figure 13**, and for a reflection phase of 0°

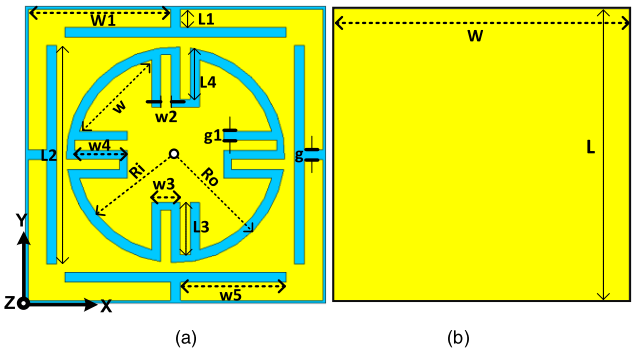

FIGURE 13. Proposed unit cell; (a) front view, (b) back view.

TABLE 3. Optimized dimensions of the unit cell.

Dimensions	Values (mm)	Dimensions	Values (mm)
L	14.8	W	14.8
L1	0.9	w1	7
L2	10.9	w2	0.50
L3	2.36	w3	1.40
L4	2.62	w4	2.60
g	0.50	w5	5.20
g1	0.45	w	5.03
Ri	4.88	Ro	5.38

at 2.45 GHz and 5.8 GHz the optimized values are given in **Table 3**. A parametric study of the unit cell is also presented to understand its operation and optimized design procedure, as illustrated in **Figure 14**.

As in the first step, a simple square patch (AMC I) is designed. It is observed that the unit cell has provided a zero-reflection phase at 3.5 GHz as shown in **Figure 15**(a). Next, a circular ring slot with outer stub slots (AMC II) are integrated into the patch to introduce a dual reflection phase. It can be realized in Figure 15 (b) that the design has produced zero-reflection phases at 2.5 GHz and 6.6 GHz. Then in the third step, an inner circular stub (AMC III) is introduced into AMC I, this is also aimed at enabling a dual reflection phase behavior. This step results into a zero-reflection phase at 2.6 GHz and 6 GHz, as illustrated in Figure 15(c). Finally, both AMC II and AMC III are combined to produce the final proposed unit cell (AMC IV). This unit cell exhibits a reflection phase of 0° at 2.45 GHz and 5.8 GHz in a miniaturized form to operate as a dual-band reflector for the proposed antenna. Simulated reflection phases for the different design steps are summarized in **Figure 15**, with a parametric study presented in the next section.

B. PARAMETRIC ANALYSIS OF THE AMC UNIT CELL

Three important parameters of the AMC unit cell are studied in this section; the width of the inner stub of the circular patch *'W4'*, the length of the stub of the square patch *'L4'*, and the gap between the slot '*g*'. Reflection phases in the lower and upper bands are monitored and optimized as shown in **Figure 16**. First, decreasing the value of '*W4*' from 2.6 mm to 0.5 mm caused in the upward phase shift of the upper frequency band from 5.8 GHz to 6.2 GHz (400 MHz). The

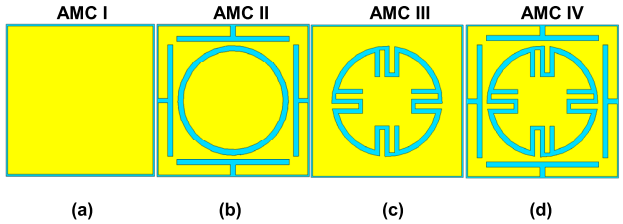

FIGURE 14. Unit cell design steps; a) patch Only (AMC I), (b) patch with slot stubs (AMC II), (c) patch with circular stubs (AMC III), (d) final design (AMC IV).

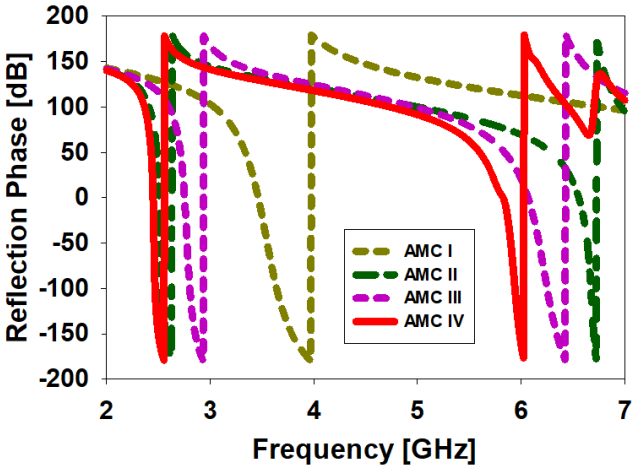

FIGURE 15. Reflection phases for the unit cell shown in Fig.14; (a) AMC I, (b) AMC II, (c) AMC III, (d) AMC IV.

lower band changed from 2.45 GHz to 2.6 GHz (150 MHz) as shown in Figure 16 (a). On the other arm, the reflection phase of the upper frequency band behaved similarly when the value of '*L4*' is reduced from 2.62 mm to 1 mm, shifting the band from 5.8 GHz to 6.3 GHz (500 MHz). A slight shift is also observed in the lower band from 2.45 GHz to 2.47 GHz (30 MHz) as shown in Figure 16 (b). It is noticed that when '*g*' is increased from 0.5 mm to 2 mm, both lower and upper bands are affected. The lower band is increased from 2.45 GHz to 2.47 GHz (30 MHz) while the upper band varied from 5.8 GHz to 5.9 GHz (100 MHz) as depicted in Figure 16(c).

The current density of the dual-band AMC unit cell is shown in **Figure 17**. Both operating bands are correlated with the two metallic stubs i.e., circular, and square. In the case of lower band (at 2.45 GHz), the current mainly flows around the outermost square stub and small amount of current through the circular stub. Since, in operating the lower frequency band, the outer square stub has major contribution. While in the case of upper frequency band (at 5.8 GHz), the current circulates the inner circular stub and some amount of current flows through the outer square stub.

C. EQUIVALENT CIRCUIT MODEL FOR THE UNIT CELL

Figure 18 shows the circuit model of the proposed AMC unit cell. A circuit model is made and simulated in Advanced

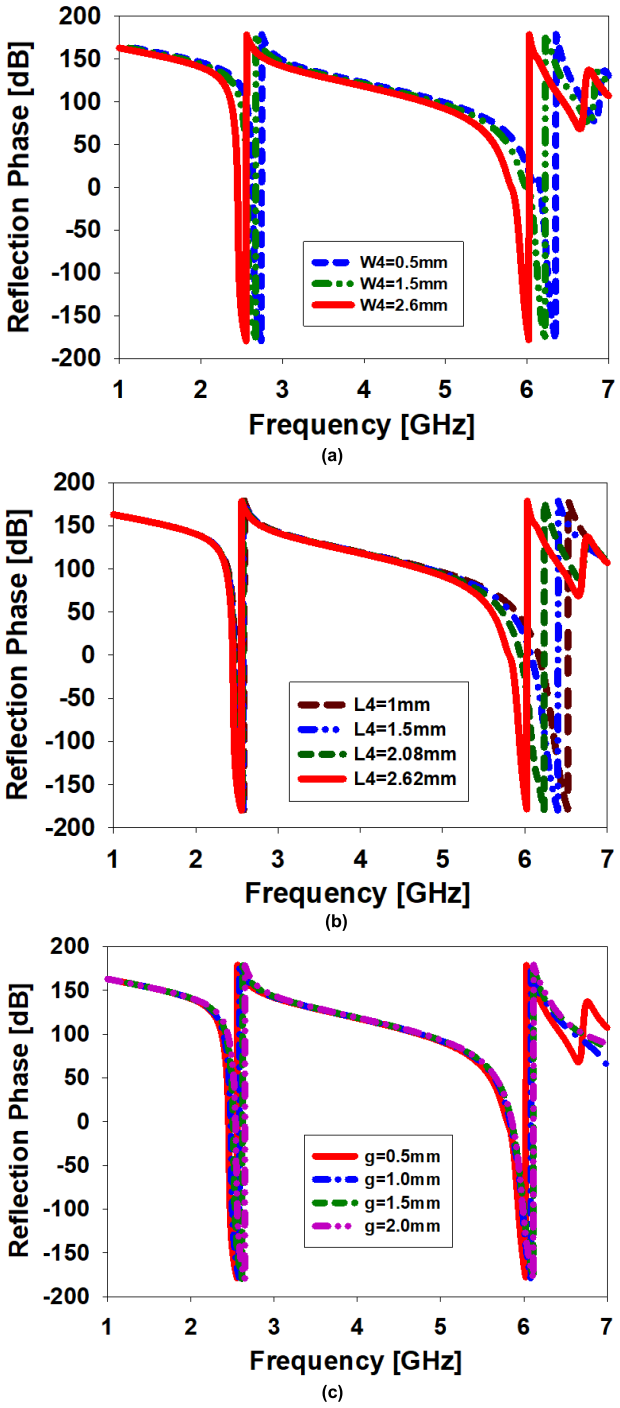

FIGURE 16. Reflection phases resulting from the AMC unit cell variations; (a) for *'W4'*, (b) for *'L4'*, (c) for *'g'*.

Design System (ADS) software, consisting of four capacitors connected in parallel with four inductors and one resistor.

The dual reflection phase behavior of this equivalent circuit can be modeled using the equivalent impedances of the circular and square patch in the unit cell, *'Zs1'* and *'Zs2'*. Their impedance is calculated as follows:

$$Zs_1 = \left[j\omega\,(C1//C2) + \frac{1}{jw(L1//L2)} \right] \tag{3}$$

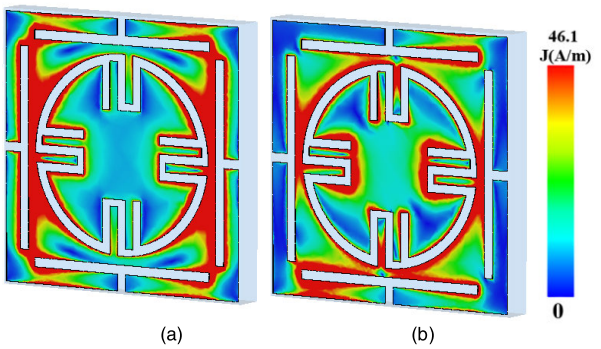

FIGURE 17. Surface current distribution the unit cell; (a) at 2.45 GHz, (b) at 5.8 GHz.

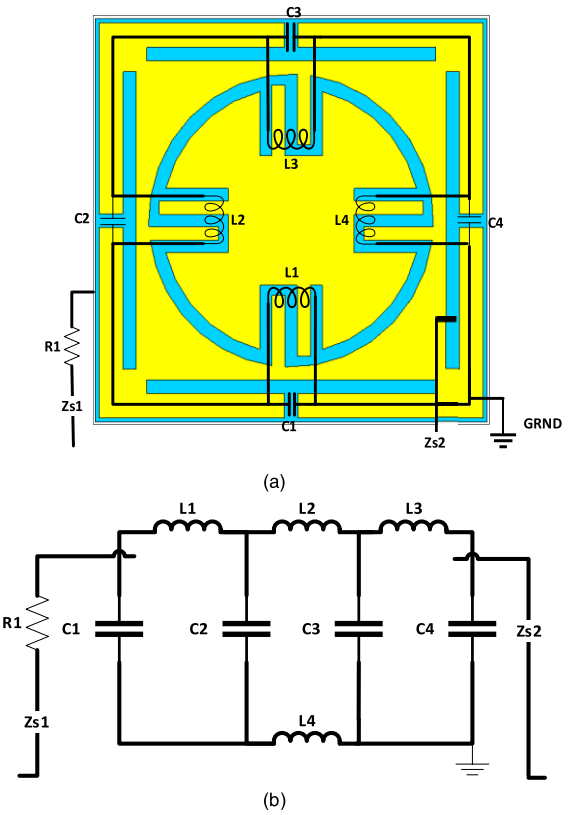

FIGURE 18. (a) Top view of dual-band AMC unit cell, (b) equivalent circuit.

and

$$Zs_2 = \left[j\omega\,(C3//C4) + \frac{1}{jw(L3//L4)} \right] \tag{4}$$

where *'L1'*, *'L2'*, *'L3'*, *and 'L4'*, are the circular patch inductances while *'C1'*, *'C2'*, *'C3'*, *and 'C4'* are the square patch capacitances, and 'ω' is the angular frequency. The unit cell is designed by means of transmission-line (TL) theory, where a circular patch and an outer square patch of the AMC act as a parallel RLC circuit. The operating frequency bands of the unit cell is calculated as follows [25]:

$$f1 = \frac{1}{2\pi\sqrt{\frac{(L2//L1)(C1.C2)}{(C1+C2)}}} \tag{5}$$

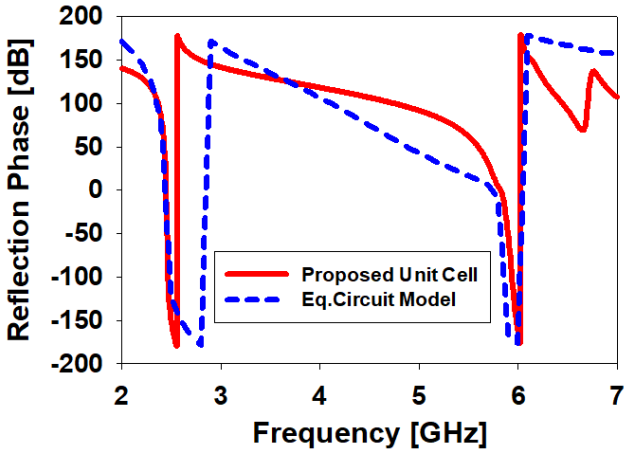

FIGURE 19. Equivalent circuit model for the proposed unit cell.

TABLE 4. List of the values for equivalent circuit model.

Inductors	Values (nH)	Capacitors	Values (pF)	Resistors/ Impedance	Values (Ω)
L1	6.1	C1	4.22	R1	21
L2	0.9	C2	1.35	Zs1	50
L3	1	C3	1.5	Zs1	50
L4	2.1	C4	45		

and

$$f2 = \frac{1}{2\pi\sqrt{\frac{(L4//L3)(C3.C4)}{(C3+C4)}}} \tag{6}$$

when *'Zs1* and *Zs2'* approaches to infinity, the dominators of (7 and 8) approaches to zero. The working frequencies and the total surface impedances of the AMC depend on the values of the lumped components which can be estimated as follows:

$$L = \mu_o \frac{h_{sub}.l_{effr}}{l1} \tag{7}$$

and

$$C = \varepsilon_o \varepsilon_r \frac{S_r}{h_{sub}} \tag{8}$$

where, 'ε_o *and* μ_o are the permittivity and the permeability in free space, 'h_{sub}' is the height of the substrate, 'ε_r is the relative permittivity of the substrate's material, and l_{effr} is the effective length of the metal. The optimized parameters of the capacitors, inductors and resistors are summarized in **Table 4**.

Figure 19 shows the comparison of the reflection phases obtained from the circuit model, simulated in ADS software (in **Figure 18**), indicates the reasonable agreements with results of the unit cell simulated in CST software. It can be noticed that both have good agreement results. The reflection phase has narrow bandwidth when it is drawn in CST while in the case of ADS the phase of the reflection coefficient has wider bandwidth as compared to CST. But both have zero-reflection phases at lower and upper bands. This validates the circuit model for the dual reflection phase AMC design.

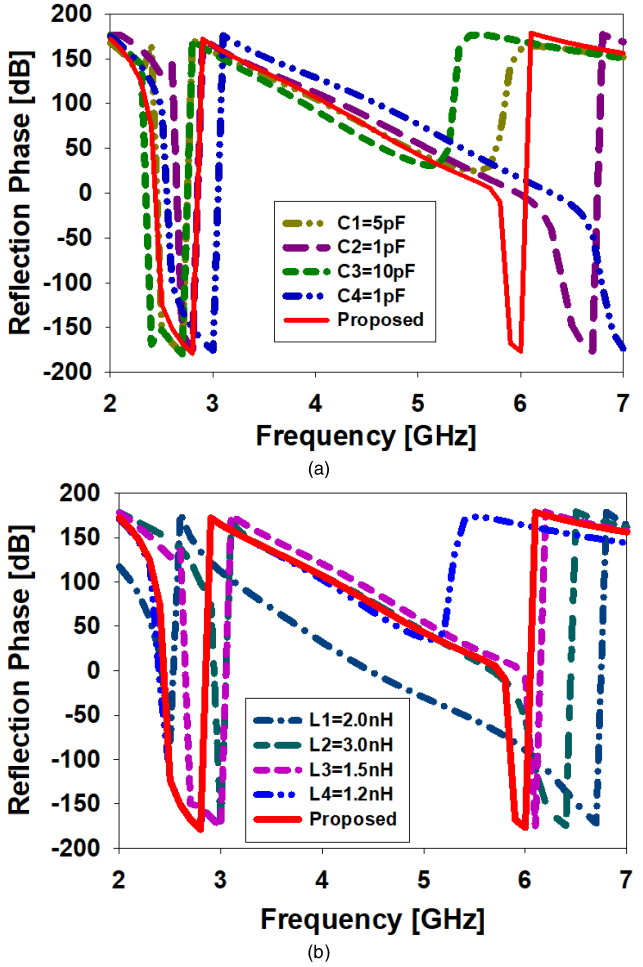

FIGURE 20. Variation in the values of lumped elements of the equivalent circuit model for the unit cell, (a) Variation in the values of the capacitors, (b) Variation in the values of the inductors.

D. PARAMETRIC ANALYSIS OF THE EQUIVALENT CIRCUIT MODEL FOR THE UNIT CELL

A parametric study of the circuit model for the unit cell is also performed to examine the *S*-parameters using the time domain solver in CST. According to (7 and 8), by changing the values of the capacitors and inductors, the operating frequency varies, as seen in **Figure 20**. From Figure 20 (a), it can be noticed that when the value of the capacitor *'C1'* is increased from 4.22 pF to 5 pF and *'C3'* from 1.5 pF to 10 pF, the circuit model provides a zero-reflection phase at the lower band but not at the upper band. Meanwhile, by reducing the values of the capacitors *'C2'* from 1.35 pF to 1 pF and *'C4'* from 45 pF to 1 pF, results in a slight variation of the reflection phase at both frequency bands. In Figure 20 (b), the variation in the values of inductors is also presented. Decreasing the value of inductor *'L1'* from 6.1 nH to 2 nH and *'L4'* from 2.1 nH to 1.2 nH provides a zero-reflection phase only at 2.45 GHz while the upper band remained the same. On the contrary, by increasing the values of the inductors *'L2'* from 0.9 nH to 1.5 nH and *'L3'* from 1 to 1.2 nH shifts the reflection phase in both frequency bands by 0.5 GHz.

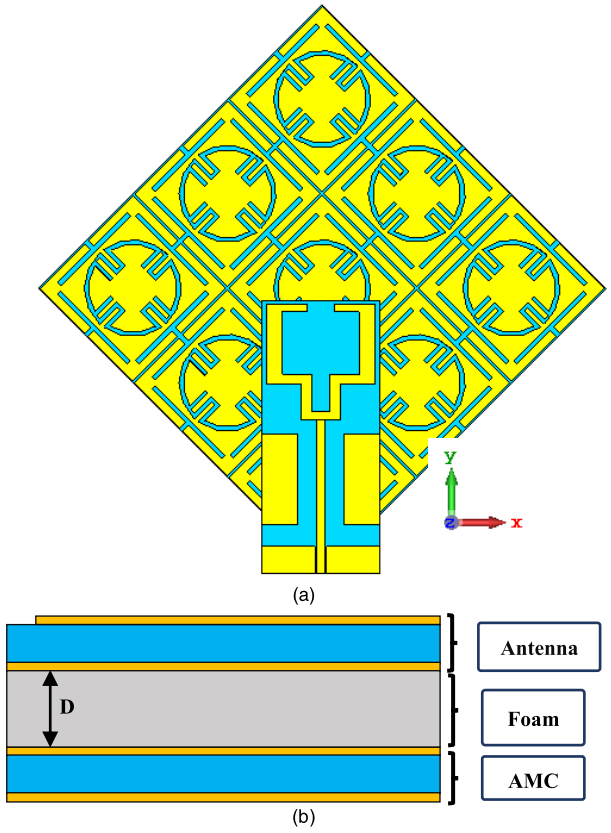

FIGURE 21. AMC-backed antenna topology in free space; (a) top View, (b) side view.

IV. AMC-BACKED ANTENNA IN FREE SPACE

To reduce the coupling towards human body, a 3 × 3 AMC-plane is enrolled as the back plane of the antenna as presented in **Figure 21**. The antenna radiator which contains a CPW feed, a ground plane and with a radiating patch to be located on top of the AMC-plane at a distance '*D*' (of 10 mm) to function as the electro-magnetic reflector. The front view and the side views are presented in Figure 21.

A. ANALYSIS OF THE AMC-BACKED ANTENNA IN FREE SPACE

When the AMC is placed at an angle of 0°, the antenna did not show any optimal performance. Therefore, it is necessary to examine the effects of the AMC arrays on the antenna's performance with different angles. The reflection coefficient [dB] of the reported AMC-backed design is studied when the AMC array is rotated at various angles i.e., 0°, 15°, 30°, 45° and 60°. Their results are summarized in **Figure 22**, indicating that the reflection coefficient of the AMC-backed antenna provided a better response except for zero-degree rotation. While in the case of other angles, the reflection coefficient is stable at both frequency bands. But it is preferred to use the angle of 45° because, in the case of the prototype, it is easy to place the AMC behind the antenna with 45° rotation. The optimal performance of the AMC placement is also found at an angle of 45°.

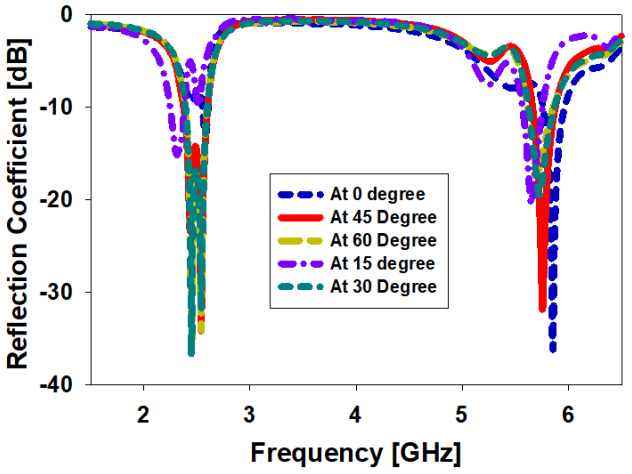

FIGURE 22. Comparison of the reflection coefficient when the AMC-backed antenna placed at different angles.

TABLE 5. Antenna gains [dB] with different number of array elements.

AMC array configurations Cells × Cells	Peak Gain of the antenna with AMC-backing [dB]	
	2.45 GHz	5.8 GHz
2 × 2	1.89	4.8
3 × 3	1.96	6.02
4 × 4	1.97	6.05

Different arrays configuration of the AMC-plane is investigated in **Figure 23**, and the resulting antenna peak gains are given in **Table 5**. It is realized that there is not much difference in terms of reflection coefficient when different array configurations are used. However, the antenna realized gain improved when the elements in the array are increased in number. Noted that there is also a minimal increase in performance when a 4 × 4 array is used in comparison with a 3 × 3 configuration.

Figure 24 illustrates that there is a minimal change in the S_{11} of the AMC-backed antenna with the variation in '*D*' (at 4, 6, 8, and 10 mm) in free space. From the graph, the antenna did not operate well at 2.45 GHz and 5.8 GHz, when the AMC is kept at 0 mm distance. However, as '*D*' is increased, the reflection coefficient started improving. The antenna featured a good S_{11} in both operating bands i.e., 2.45 GHz and 5.8 GHz when placed at a distance of 10 mm. $|S_{11}|$ is improved by increasing the distance of '*D*' as can be seen in Figure 24.

B. MEASUREMENT OF FABRICATED PROTOTYPE AMC-BACKED ANTENNA IN FREE SPACE

The fabricated prototype of the 3 × 3 AMC-backed antenna is depicted in **Figure 25**. To ensure consistency in the distance '*D*' between the dual-band antenna and the AMC-plane during measurements, a 10 mm thick foam layer is used. A vector network analyzer (VNA) E5071C is utilized to check the S_{11} of the antenna with AMC-backing. The radiation pattern is evaluated in an anechoic chamber and its evaluation setup is presented in Figure 25 (b).

The comparison of S_{11} of the antenna with AMC-backing and without AMC-backing is simulated and measured in

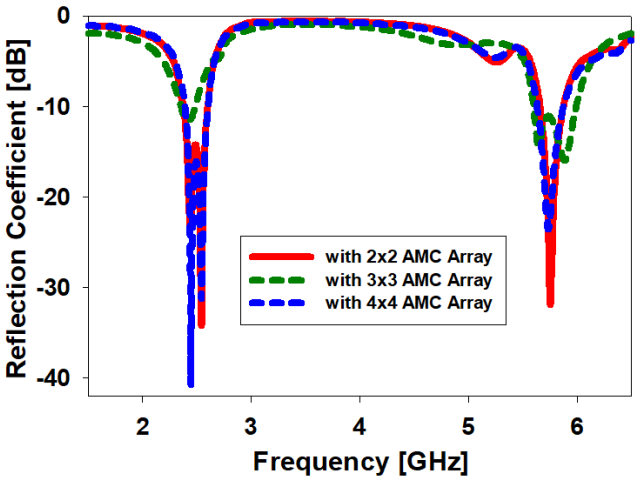

FIGURE 23. S_{11} behavior of the AMC-backed antenna with different number of array elements.

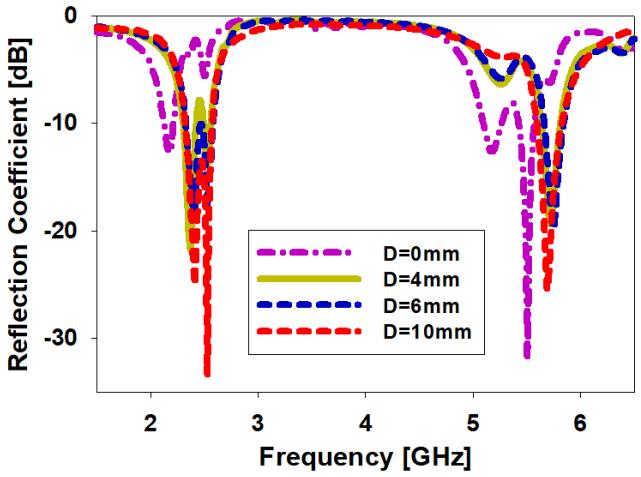

FIGURE 24. Comparison of S_{11} with different values of distance '*D*'.

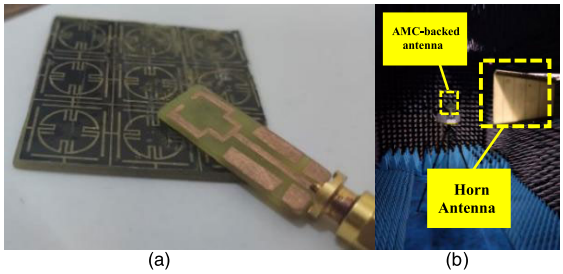

FIGURE 25. (a) Fabricated prototype of the AMC-backed antenna in Free space, (b) its evaluation setup in an anechoic chamber.

Figure 26, indicating the consistency with each other. Simulated reflection coefficients showed operation in the frequency ranges of 2.36 to 2.6 (9.8%) in the lower band, and from 5.66 to 5.90 (4.13%) in the upper band. In the measurements, the antenna with AMC-backing in free space operated within the bandwidths from 2.365 to 2.595 GHz (9.38%) at 2.45 GHz, and from 5.45 to 5.94 GHz (8.44%) at 5.8 GHz.

Figure 27 presents the *xz*-, and *yz*- planes of the simulated and measured radiation pattern in free space. The patterns

TABLE 6. Antenna gains (dB) and efficiencies (%) with and without AMC.

Frequency (GHz)	Without AMC		With AMC	
	Gain (dB)	Efficiency (%)	Gain (dB)	Efficiency (%)
2.45	0.574	71	4.92	68
5.8	3.84	67	4.76	63

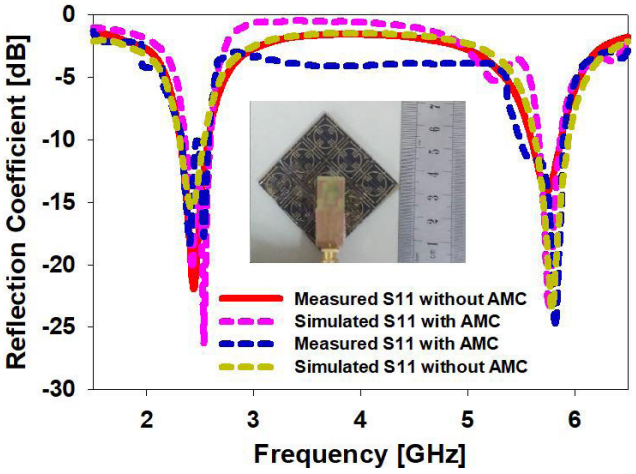

FIGURE 26. Comparison between the simulation and measurement results of S_{11} of the antenna without and with AMC in free space.

showed an elliptical radiation characteristic at 2.45 GHz, and a directional radiation characteristic at 5.8 GHz. The red colored (dash-dotted) line indicates the measured radiation pattern and black colored (solid) line shows the simulated radiation pattern at *xz*- and *yz*-planes. The simulated peak gains of the antenna are found to be 1.89 dB at 2.45 GHz and 6.02 dB at 5.8 GHz. While the measured gains of the AMC-backed antenna in free space are calculated as 1.78 dB at 2.45 GHz and 5.97 dB at 5.8 GHz. The efficiency and the gain of the antenna with and without AMC-plane are depicted in **Table 6**.

Figure 28 explains the flow of current throughout the surface of the proposed antenna with AMC-backing at lower and upper bands. As it is observed that the surface current in the lower band mainly flows around the 2 × 2 AMC array and from both resonators of the antenna. While in the case of upper band, current flows throughout the AMC-backed CPW fed antenna as well as through the discrete ground circular rings. There is more evident difference in terms of current density on the AMC-plane at 2.45 GHz and 5.8 GHz, as presented in Figure 28. For example, there is a dense current distribution on almost all unit cells in the upper band, whereas in the lower band, the current circulates around the lower 2 × 2 array under the CPW radiator.

V. AMC-BACKED ANTENNA WITH HUMAN PROXIMITY

To explore the appropriateness of the antenna with AMC-backing for off-body IoT applications, the proposed design is simulated on human body phantom model in this section. Consequently, to design an antenna for the applications in

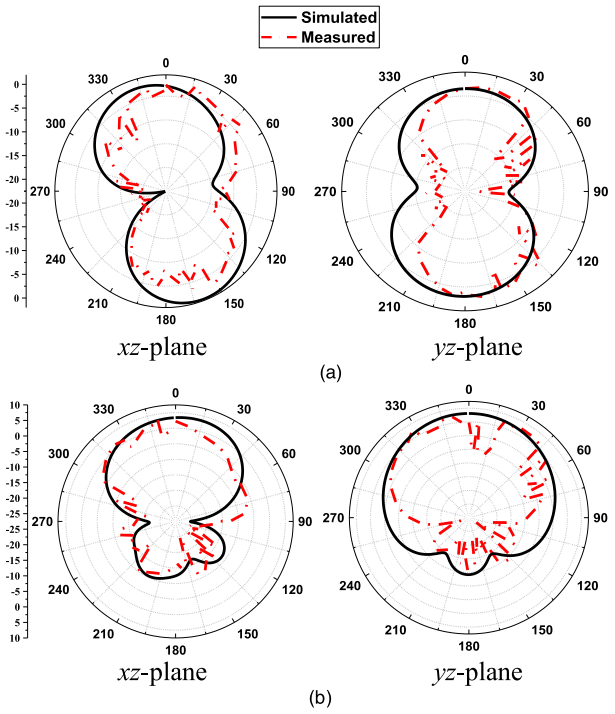

FIGURE 27. Comparison of the simulated and measured 2D radiation patterns of the AMC-backed antenna in free space (a) at 2.45 GHz, (b) at 5.8 GHz.

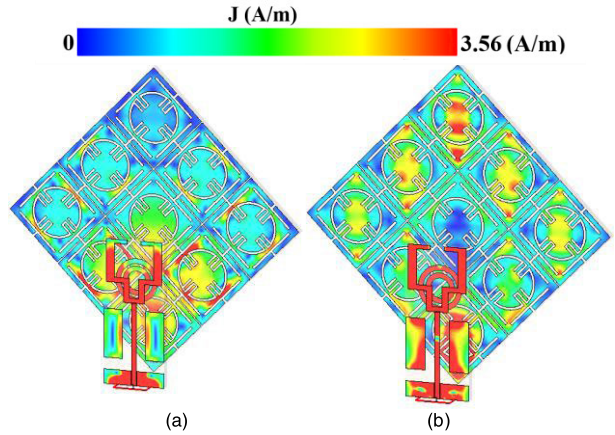

FIGURE 28. Surface current distribution of the AMC-backed antenna in free space (a) at 2.45 GHz, (b) at 5.8 GHz.

BCC that had high precision and the presence of the human body phantoms must take into consideration while calculating SAR. For that the antenna performance in proximity of human phantoms and the SAR values at 2.45 GHz and 5.8 GHz are evaluated.

A. HUMAN PROXIMITY EFFECTS

In an ideal case, off-body IoT-based antennas should be planned to avoid significant coupling effects from the human tissues. To estimate these effects, the reported design with AMC and without AMC is kept at 1 mm spacing over a 100 mm × 100 mm various layers of tissues. It consists of a layer of denim (0.6 mm-thick), skin (1.6 mm-thick), fat

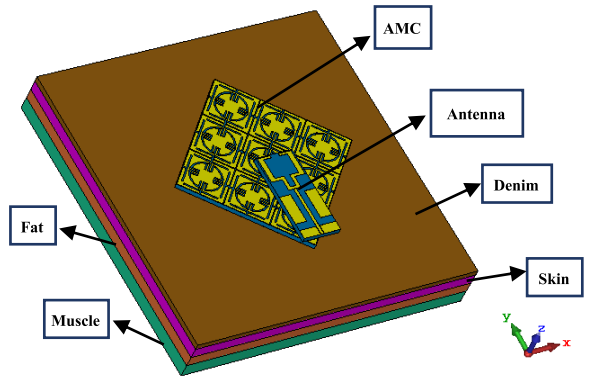

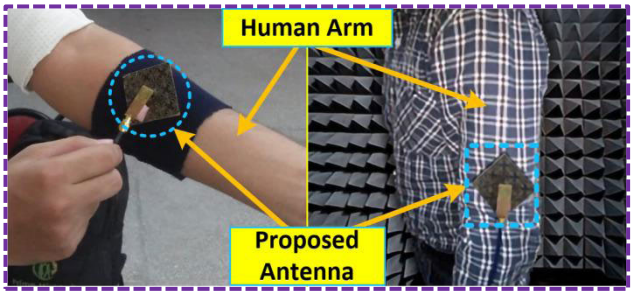

FIGURE 29. AMC-backed antenna placed on human arm model, (a) 3D layer model of human tissues, (b) antenna tested on human arm in free space, (c) antenna tested on human arm inside chamber.

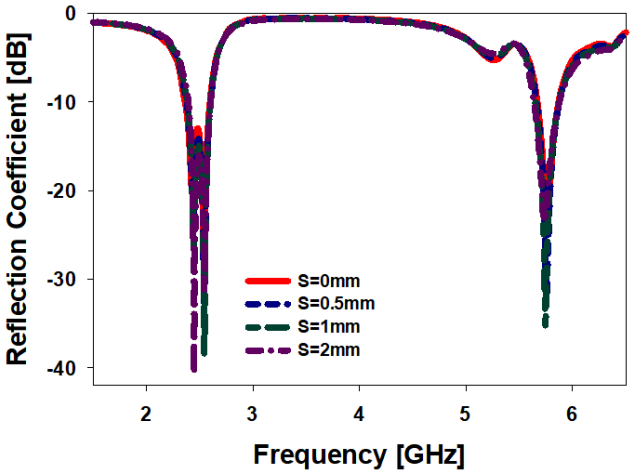

FIGURE 30. Comparison of the different values of '*S*' between the AMC-backed antenna and the different tissue layers.

(2-mm thick), and muscle (5 mm-thick) tissue as shown in the **Figure 29.** The properties of the different tissue layers are listed in **Table 7**. The spacing '*S*' among the antenna with AMC-backing and the human tissues is increased to further investigate the contribution of the AMC when used on the human phantom as presented in **Figure 30**.

The S_{11} of the antenna with AMC-backing in free space as well as on human phantoms are simulated and measured in **Figure 31.** Simulations on the human tissues indicate that the AMC-backed antenna operates from 2.32 to 2.57 (10.2%)

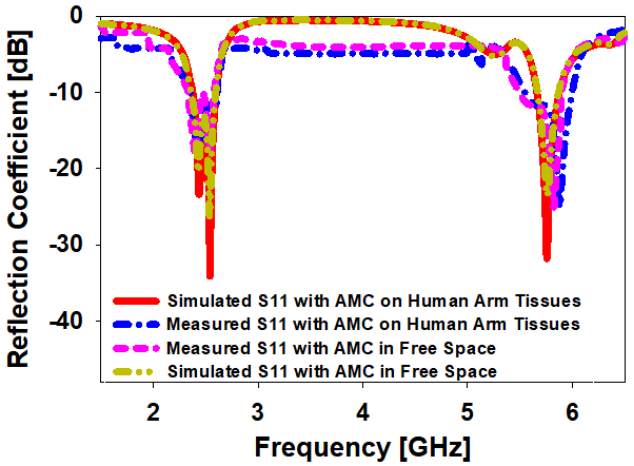

FIGURE 31. Comparison of the simulated and measured reflection coefficients of the AMC-backed antenna in free space and on human arm tissues.

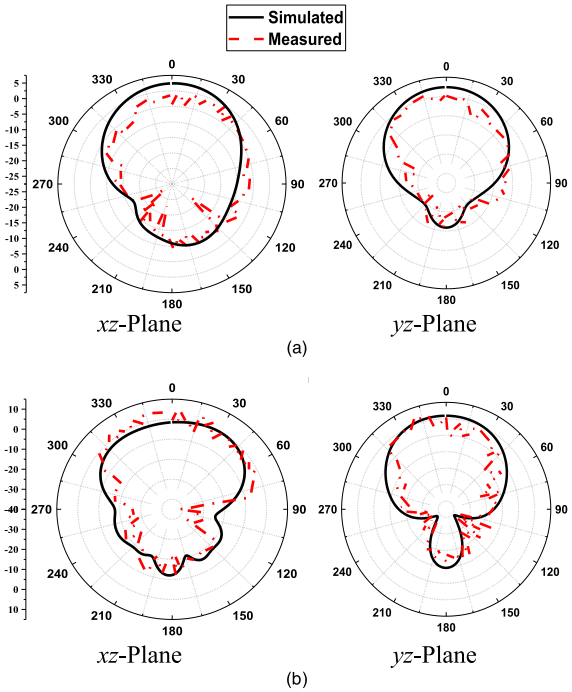

FIGURE 32. Simulated and measured 2D radiation patterns of the AMC-backed antenna on human arm (a) at 2.45 GHz, (b) at 5.8 GHz.

TABLE 7. Properties of the different tissue layers [17].

Layers	Permittivity	Conductivity (S/m)	Density (kg/m^3)
Denim	1.781	0.083	751
Skin	41.42	0.89	1121
Fat	5.45	0.049	780
Muscle	54.88	0.959	1121

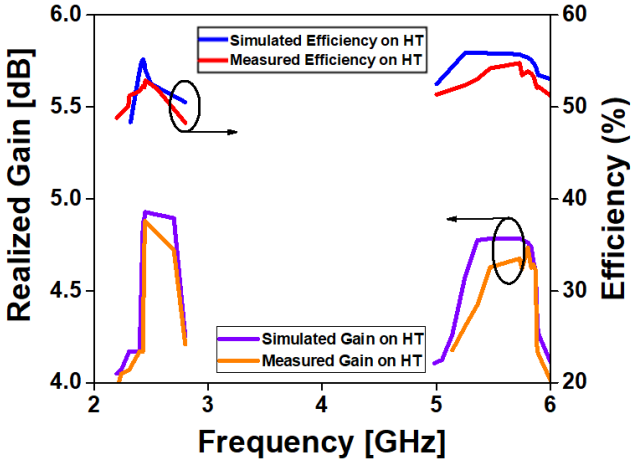

FIGURE 33. Simulated and measured realized gain and efficiency of the AMC-backed antenna on human tissues.

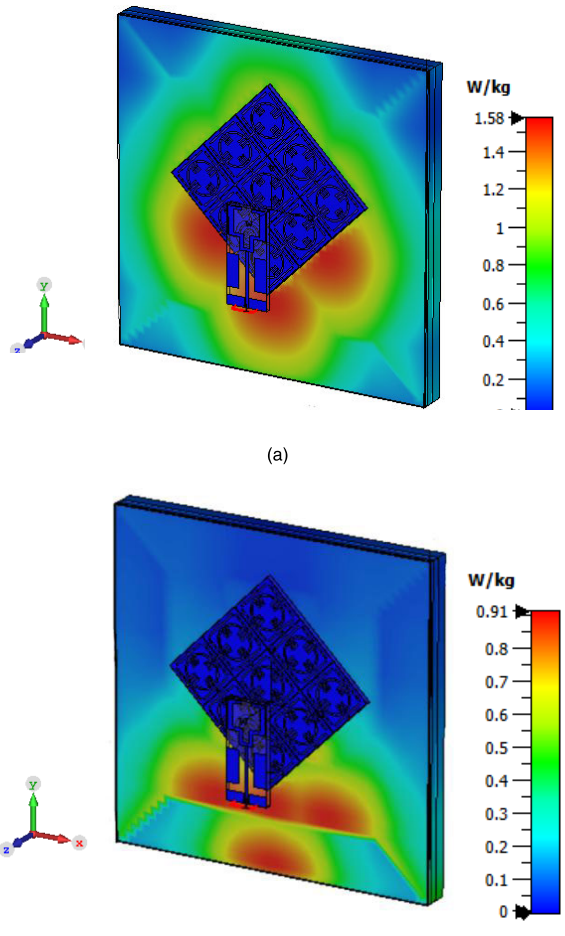

FIGURE 34. SAR distribution of the antenna with AMC-backing placed at 1 mm from the phantom; (a) at 2.45 GHz, (b) at 5.8 GHz.

in the lower band and from 5.59 to 5.83 (4.14%) in the upper band. The fabricated antenna on the phantom, on the other arm, featured bandwidths from 2.325 to 2.56 GHz (9.6%) at 2.45 GHz and from 5.43 to 6.15 GHz (12.4%) at 5.8 GHz. This proves that the simulated results have perfect agreement with the measured ones.

Figure 32 presents the *xz*-, and *yz*-planes of the simulated and measured radiation pattern on human arm tissues. These far-field results prove that the antenna with AMC-backing has directional radiation pattern at both frequency bands under the proximity of human tissues. Simulation results also have shown on-arm realized gains of 4.92 dB in the

TABLE 8. Comparison of this work with the previous relevant research work.

Ref. No.	Dimensions (mm^3)/ ($\lambda_g{}^3$) (λ_g: Guided wavelength @2.45 GHz)	Operating Frequency (GHz)	Peak Gain (dB)	Antenna Type	Substrate Material	SAR (W/kg)/ @ 10g	Bandwidth (%)
[7]	(30×45×3.2) / (0.514×0.77×0.054)	2.4/5.8	0.56/-1.59	Patch	FR-4 (lossy)	Not Calculated	4.9/2.8
[8]	(50×50×0.6) / (0.856×0.856×0.01)	2.45/5.8	1.2/7.9	Patch	FR-4 (lossy)	0.81/0.24	4.2/10.5
[11]	(80×80×8.6) / (0.71×0.71×0.076)	2.45	<6	Microstrip Patch	Felt	Not Calculated	4.49
[13]	(75.7×75.7×0.1) / (1.05×1.05× 0.0014)	2.45	6.584	Circular Slotted Patch	Roger 3850 ULTRALAM	0.18 @ 1g	6.53
[15]	(60×60×1.57) / (1.03×1.03×0.027)	1.9/2.45	4.0/4.3	Circular	FR-4 (lossy)	Not Calculated	1.8/2.4
[16]	(70×70×3) / (0.69×0.69×0.029)	2.45/3.5	6	Rectangular	Felt	Not Calculated	5.3/3.14
[17]	(80×92×2) / (0.75×0.86×0.018)	2 / 5.8	8.26/9.86	Patch	Felt	Not Calculated	9.48
[18]	(100×100×3.2) / (1.33×1.33×0.042)	2.45/5.8	1.9/5.9	Circular	F4B	0.254/0.074 @ 1g	2.57/5.22
[19]	(100×100×2) / (0.9×0.9×0.018)	2.45/5.8	6.33/6.98	Circular	Felt	0.042/0.09 @ 1g	4.9/3.8
[20]	(130.8×130.8×3.04) / (1.05×1.05×0.024)	1.575/2.45	5.1/5.03	Diamond Shape	Roger 3003C	0.04/0.043	1.84/0.736
[23]	(44×44×1.6) / (0.75×0.75×0.027)	3.5	5.62	Circular & Square	FR-4 (lossy)	Not calculated	16.36
[24]	(83.8×83.8×1.6) / (1.42×1.42×0.027)	2.6	7.02	Monopole Radiator	FR-4 (lossy)	Not calculated	26.45
[25]	(36×40×1.6) / (0.61×0.61×0.027)	3.27/5.11	6.46/7.12	Patch	FR-4 (lossy)	Not calculated	12.23/21.96
[This Paper]	**(44.4×44.4×1.6) / (0.75×0.75×0.027)**	**2.45/5.8**	**Sim: 4.92/4.76 Meas:4.88/4.73**	**Simple Monopole**	**FR-4 (lossy)**	**1.58/ 0.91**	**Sim:10.2/4.14 Meas: 9.6/12.4**

lower band (at 2.45 GHz) and 4.76 dB in the upper band (at 5.8 GHz), whereas measurement results give the realized gain of 4.88 dB in the lower band (at 2.45 GHz) and 4.73 dB in the upper band (at 5.8 GHz). While the total radiation measured efficiency is found to be more than 53% when the AMC-backed antenna is placed over human tissues (HT). The simulation and measurement graphs for the gain and the efficiency are presented in **Figure 33.** The comparison of this work with the previous relevant research work is presented in **Table 8**.

B. SPECIFIC ABSORPTION RATE (SAR) ANALYSIS

The radiations of electromagnetic waves may cause health risks to human body and such risks are calculated in terms of SAR. The relationship between the input power and the SAR is as follows [22]:

$$\text{SAR} = \frac{\sigma |E^2|}{\rho} \tag{9}$$

where 'σ' and 'ρ' denotes the thermal conductivity (S/m) and the mass density (kg/m^3), while 'E' is the electric field intensity (V/m). The electric power intensity is related to the signal power as below:

$$\text{Power}(\text{W/m}^2) = \frac{(\text{E(V/m)})^2}{377} \tag{10}$$

The simulation results are carried out to calculate SAR when the AMC-backed antenna is kept at 1 mm of distance to the human arm model. Input power 'P_{in}' is kept constant at 0.5 W, with the SAR values are evaluated based on IEEE/IEC 6270-1 standards, averaged over 10 grams of tissue mass. Calculated SAR values are 1.58 W/kg at 2.45 GHz and 0.91 W/kg at 5.8 GHz over 10 g as presented in **Figure 34**. The simulated SAR values are less than the limit of 2 W/kg over 10 grams of the human tissues, indicating the capability of the reported AMC-plane in decreasing the electromagnetic absorptions by the human arm. Figure 34 presents the distributions of the SAR when the antenna is kept at 1 mm away from human arm tissues. SAR will be reduced more when we increase the gap among the human tissues and the antenna with AMC-backing.

VI. CONCLUSION

A novel IoT-based antenna with AMC-backing for off-body devices working at 2.45 GHz and 5.8 GHz bands is presented monopole radiating patch, which is then integrated with a 3 × 3 AMC-plane to decrease the backward radiation and to in this research. The antenna consists of a CPW-fed planar reduce the coupling effects on human body in IoT applications. The unit cells of the AMC are designed based on rectangular and circular stubs. The rectangular stubs generate a zero-reflection phase at the lower frequency band (2.45 GHz), whereas the circular stubs are used to generate another zero-reflection phase at the upper-frequency band (5.8 GHz). Both antenna and AMC-plane layers are designed using a single 1.6 mm-thick FR-4 substrate with a compact size of 44.4 mm × 44.4 mm × 1.6 mm ($0.75\lambda_g \times 0.75\lambda_g \times 0.027\lambda_g$). Satisfactorily measured bandwidths of 9.6% and 12.4% are achieved in the lower and the upper

bands, correspondingly, with measured peak gains of 4.88 dB (at 2.45 GHz) and 4.73 dB (at 5.8 GHz). Calculated SAR on a three-layered human phantom is observed to be 1.58 W/kg at 2.45 GHz and 0.91 W/kg at 5.8 GHz. Experimental evaluations also indicate that the performance of the proposed antenna with compact size is suitable for off-body IoT devices.

REFERENCES

[1] P. Sambandam, M. Kanagasabai, R. Natarajan, M. G. N. Alsath, and S. Palaniswamy, "Miniaturized button-like WBAN antenna for off-body communication," *IEEE Trans. Antennas Propag.*, vol. 68, no. 7, pp. 5228–5235, Jul. 2020.

[2] R. Joshi, E. F. N. M. Hussin, P. J. Soh, M. F. Jamlos, H. Lago, A. A. Al-Hadi, and S. K. Podilchak, "Dual-band, dual-sense textile antenna with AMC backing for localization using GPS and WBAN/WLAN," *IEEE Access*, vol. 8, pp. 89468–89478, 2020.

[3] S. N. Mahmood, A. J. Ishak, A. Ismail, A. C. Soh, Z. Zakaria, and S. Alani, "ON-OFF body ultra-wideband (UWB) antenna for wireless body area networks (WBAN): A review," *IEEE Access*, vol. 8, pp. 150844–150863, 2020.

[4] K. Turbic, M. Sarestoniemi, M. Hamalainen, and L. M. Correia, "User influence on polarization characteristics in off-body channels," *IEEE Access*, vol. 8, pp. 167570–167584, 2020.

[5] R. B. V. B. Simorangkir, Y. Yang, K. P. Esselle, L. Matekovits, and S. M. Abbas, "A simple dual-band dual-mode antenna for off-/on-body centric communications," in *Proc. 10th Eur. Conf. Antennas Propag. (EuCAP)*, Apr. 2016, pp. 1–5.

[6] H. Sun, Y. Hu, R. Ren, L. Zhao, and F. Li, "Design of pattern-reconfigurable wearable antennas for body-centric communications," *IEEE Antennas Wireless Propag. Lett.*, vol. 19, no. 8, pp. 1385–1389, Aug. 2020.

[7] J. Tak, S. Woo, J. Kwon, and J. Choi, "Dual-band dual-mode patch antenna for on-/off-body WBAN communications," *IEEE Antennas Wireless Propag. Lett.*, vol. 15, pp. 348–351, 2016.

[8] C. Zhao and W. Geyi, "Design of a dual band dual mode antenna for on/off body communications," *Microw. Opt. Technol. Lett.*, vol. 62, no. 1, pp. 514–520, Jan. 2020.

[9] T. Rashid, M. N. Hasan, and P. S. Mazumdar, "An L-slot compact antenna for medical, wearable device and IoT applications," in *Proc. Int. Conf. Inf. Commun. Technol. Sustain. Develop. (ICICT4SD)*, Feb. 2021, pp. 100–104.

[10] D. Ali, T. Elwi, and S. Özbay, "Metamaterial-based printed circuit antenna for biomedical applications," *Eur. J. Sci. Technol.*, vol. 26, pp. 12–15, Jun. 2021.

[11] C. Mendes and C. Peixeiro, "A dual-mode single-band wearable microstrip antenna for body area networks," *IEEE Antennas Wireless Propag. Lett.*, vol. 16, pp. 3055–3058, 2017.

[12] S. Alhuwaidi and T. Rashid, "A novel compact wearable microstrip patch antenna for medical applications," in *Proc. Int. Conf. Commun., Signal Process., their Appl. (ICCSPA)*, Mar. 2021, pp. 1–6.

[13] M. El Atrash, O. F. Abdalgalil, I. S. Mahmoud, M. A. Abdalla, and S. R. Zahran, "Wearable high gain low SAR antenna loaded with backed all-textile EBG for WBAN applications," *IET Microw., Antennas Propag.*, vol. 14, no. 8, pp. 791–799, Jul. 2020.

[14] A. Y. I. Ashyap, S. H. B. Dahlan, Z. Z. Abidin, M. H. Dahri, H. A. Majid, M. R. Kamarudin, S. K. Yee, M. H. Jamaluddin, A. Alomainy, and Q. H. Abbasi, "Robust and efficient integrated antenna with EBG-DGS enabled wide bandwidth for wearable medical device applications," *IEEE Access*, vol. 8, pp. 56346–56358, 2020.

[15] M. M. Khan, M. A. Rahman, M. A. Talha, and T. Mithila, "Wearable antenna for power efficient on-body and off-body communications," *J. Electromagn. Anal. Appl.*, vol. 6, no. 9, pp. 238–243, 2014.

[16] H. A. Mashaghba, H. A. Rahim, P. J. Soh, M. Abdulmalek, I. Adam, M. Jusoh, T. Sabapathy, M. N. M. Yasin, and K. N. A. Rani, "Bending assessment of dual-band split ring-shaped and bar slotted all-textile antenna for off-body WBAN/WLAN and 5G applications," in *Proc. 2nd Int. Conf. Broadband Commun., Wireless Sensors Powering (BCWSP)*, Sep. 2020, pp. 1–5.

[17] F. Khajeh-Khalili, A. Shahriari, and F. Haghshenas, "A simple method to simultaneously increase the gain and bandwidth of wearable antennas for application in medical/communications systems," *Int. J. Microw. Wireless Technol.*, vol. 13, no. 4, pp. 374–380, May 2021.

[18] L. Zhou, S.-J. Fang, and X. Jia, "A compact dual-band and dual-polarized antenna integrated into textile for WBAN dual-mode applications," *Prog. Electromagn. Res. Lett.*, vol. 91, pp. 153–161, 2020.

[19] L. Zhou, S. Fang, and X. Jia, "Dual-band and dual-polarised circular patch textile antenna for on-/off-body WBAN applications," *IET Microw., Antennas Propag.*, vol. 14, no. 7, pp. 643–648, Jun. 2020.

[20] K. N. Paracha, S. K. A. Rahim, P. J. Soh, M. R. Kamarudin, K.-G. Tan, Y. C. Lo, and M. T. Islam, "A low profile, dual-band, dual polarized antenna for indoor/outdoor wearable application," *IEEE Access*, vol. 7, pp. 33277–33288, 2019.

[21] C. A. Chuquitarco-Jimenez, E. Antonino-Daviu, and M. Ferrando-Bataller, "Dual-band antenna with AMC for wearable applications," in *Proc. 15th Eur. Conf. Antennas Propag. (EuCAP)*, Mar. 2021, pp. 1–4.

[22] B. Yin, M. Ye, Y. Yu, and J. Gu, "A dual-band, miniaturized, AMC-based wearable antenna for health monitoring applications," *Prog. Electromagn. Res. C*, vol. 112, pp. 165–177, 2021.

[23] M. Ameen and R. Chaudhary, "Metamaterial circularly polarized antennas: Integrating an epsilon negative transmission line and single split ring-type resonator," *IEEE Antennas Propag. Mag.*, vol. 63, no. 4, pp. 60–77, Aug. 2021.

[24] M. Ameen, O. Ahmad, and R. K. Chaudhary, "Wideband circularly-polarised high-gain diversity antenna loaded with metasurface reflector for small satellite applications," *Electron. Lett.*, vol. 55, no. 15, pp. 829–831, Jul. 2019.

[25] M. Ameen, A. Mishra, and R. K. Chaudhary, "Dual-band CRLH-TL inspired antenna loaded with metasurface for airborne applications," *Microw. Opt. Technol. Lett.*, vol. 63, no. 4, pp. 1–8, 2020.

SAROSH AHMAD (Student Member, IEEE) received the bachelor's degree in electrical engineering with specialization in telecommunication from the Department of Electrical Engineering and Technology, Government College University Faisalabad (GCUF), Pakistan, in 2021. He is currently pursuing the master's degree in advanced communication technology with the Department of Signal Theory and Communications, Universidad Carlos III de Madrid (UC3M), Madrid, Spain. He has published ten conference articles, five high indexed international journals, and four book chapters by Springer. His research interests include radio-frequency (RF) circuit design, radio-frequency identification (RFID), signals and systems, wearable and flexible antennas, metamaterial-based antennas, implantable antennas, multi-input-multi-output (MIMO) antennas, mm-wave antennas, 5G antennas, antenna arrays, dielectric resonator antennas (DRAs), photonic antennas, fluidic antennas, antenna for the Internet of Things applications, ultra-wideband (UWB) antennas, wideband antennas, reconfigurable antennas, substrate integrated waveguide (SIW) antennas, circularly polarized antennas, terahertz antennas, rectennas for energy harvesting applications, bandpass filters, half- and full-wave filter antennas, active sensors, and the IoT-based communication devices. He is a member of the IEEE Antennas and Propagation Society (APS). During his graduation, he received the fully funded PEEF Scholarship Award from the Prime Minister of Pakistan and the Silver Medal in his bachelor's program. During his volunteer-ship, he contributed himself as a Branch Treasurer at the IEEE GCUF, Faisalabad Subsection, for two years. After the graduation, he again received the fully funded Erasmus Grant Scholarship for his master's program in Madrid. During his graduation research period, he has participated in four international IEEE conferences over the world, where he has presented ten articles mostly in oral presentations. He has presented his two articles in the International Turkish Conferences where he has got the Best Paper Award and his one article in the International Moroccan Conference Proceedings.

KASHIF NISAR PARACHA (Senior Member, IEEE) received the B.S. degree (Hons.) in electrical engineering (EE) from the University of Engineering and Technology (UET), Taxila, Pakistan, in 2004, the M.S. degree in electrical engineering from the King Fahd University of Petroleum and Minerals (KFUPM), Dahran, Saudi Arabia, in 2008, and the Ph.D. degree from the Wireless Communication Center (WCC), Electrical Engineering Department (FKE), Universiti Teknologi Malaysia (UTM), Johor Bahru, Malaysia. He was a Research Assistant with the EE Department, KFUPM, from 2006 to 2008, and taught at the EE Department, The University of Faisalabad (TUF), Pakistan, from 2008 to 2011. He has been serving as an Assistant Professor with the EE Department, Government College University Faisalabad (GCUF), since 2011. He has published more than 14 journal articles and technical proceedings on antenna design, stochastic algorithms, and renewable energy resources, in international journals and conferences. His research interests include signal processing and algorithms, communication systems, antenna design, metamaterials, and renewable energy resources. He is a Life Time Professional Member of the Pakistan Engineering Council (PEC).

YAWAR ALI SHEIKH received the B.E. and M.S. degrees in electrical engineering from Air University, Islamabad, Pakistan, and the Ph.D. degree in information and communication engineering from the University of Science and Technology of China, Hefei, China. He is currently an Assistant Professor with the Department of Electrical Engineering and Technology, Government College University Faisalabad, Pakistan. His current research interests include array signal processing, speech signal processing, image processing, and antenna designing.

ADNAN GHAFFAR received the B.Sc. degree in computer engineering from BZU Multan, Pakistan, in 2010, and the M.E. degree in circuits and systems from Lanzhou Jiaotong University, Lanzhou, China, in 2015. He is currently pursuing the Ph.D. degree in electrical and electronics engineering with the Auckland University of Technology, Auckland, New Zealand. His research interests include RF circuits, reconfigurable antenna, embedded systems, metasurface antennas, and flexible and wearable antenna design.

ARSLAN DAWOOD BUTT received the B.Sc. degree (Hons.) in electrical engineering from the EME College, NUST, Pakistan, in 2010, and the M.Sc. degree in electronic systems engineering and the Ph.D. degree (Hons.) in silicon-based radiation detection systems from the Politecnico di Milano, Italy, in 2012 and 2016, respectively. During his M.S. and Ph.D. programs, he worked on international projects sponsored by the European Space Agency, the European Commission, and the Instituto Nazionale di Fisica Nucleare (INFN) Milan Section. In 2017, he joined the Department of Electrical Engineering, Government College University Faisalabad, as an Assistant Professor to pursue a career of teaching and research in Pakistan. In GCUF, he has changed his field of research to motion tracking and wearable sensors for augmented reality applications. He is the author and coauthor of about 16 research journal articles and 40 conference articles.

MOHAMMAD ALIBAKHSHIKENARI (Member, IEEE) was born in Mazandaran, Iran, in February 1988. He received the Ph.D. degree (Hons.) in electronic engineering from the University of Rome "Tor Vergata," Italy, in February 2020. He was a Ph.D. Visiting Researcher with the Chalmers University of Technology, Sweden, in 2018. His training during the Ph.D. included a research stage in the Swedish company Gap Waves AB. He is currently with the Department of Signal Theory and Communications, Universidad Carlos III de Madrid, Spain, as a Principal Investigator of the CONEX-Plus Talent Training Program and Marie Sklodowska-Curie Actions. His research interests include antennas and wave-propagations, metamaterials and metasurfaces, synthetic aperture radars (SAR), multiple-input multiple output (MIMO) systems, RFID tag antennas, substrate integrated waveguides (SIWs), impedance matching circuits, microwave components, millimeter-waves and terahertz integrated circuits, and electromagnetic systems. The above research lines have produced more than 130 publications on international journals, presentations within international conferences, and book chapters with a total number of the citations more than 2100 and H-index of 35. He was a recipient of the Three Years Research Grant funded by the Universidad Carlos III de Madrid, the European Union's Horizon 2020 Research and Innovation Program under the Marie Sklodowska-Curie Grant started in July 2021, the Two Years Research Grant funded by the University of Rome "Tor Vergata" started in November 2019, the Three Years Ph.D. Scholarship funded by the University of Rome "Tor Vergata" started in November 2016, and two young engineer awards of the 47th and 48th European Microwave Conference held in Nuremberg, Germany, in 2017, and in Madrid, Spain, in 2018. His research article entitled "High-Gain Metasurface in Polyimide On-Chip Antenna Based on CRLH-TL for Sub Terahertz Integrated Circuits" published in *Scientific Reports* was awarded as the Best Month Paper at the University of Bradford, in April 2020. He is serving as an Associate Editor for *Journal of Engineering* (IET) and the *International Journal of Antennas and Propagation*. He also acts as a referee in several highly reputed journals and international conferences.

PING JACK SOH (Senior Member, IEEE) was born in Sabah, Malaysia. He received the B.Eng. and M.Eng. degrees in electrical engineering (telecommunication) from Universiti Teknologi Malaysia (UTM) in 2002 and 2006, respectively, and the Ph.D. degree in electrical engineering from KU Leuven, Belgium, in 2013.

He is currently an Associate Professor with the School of Computer and Communication Engineering (SCCE), Universiti Malaysia Perlis (UniMAP), and a Research Affiliate with KU Leuven, Belgium. From 2002 to 2004, he was a Test Engineer with Venture Corporation. In 2005, he joined Motorola Solutions Malaysia as an Research and Development Engineer, where, he worked on the characterization and testing of new two-way radios' antennas and RF front-ends. In 2006, he joined SCCE-UniMAP as a Lecturer, and served as the Deputy Director for the Centre for Industrial Collaboration (CIC) from 2007 to 2009. He went on leave from UniMAP in 2009 to pursue his Ph.D. and research attachment in KU Leuven, Belgium. He was first a Research Assistant (from 2009 to 2013) and then a Postdoctoral Research Fellow (from 2013 to 2014). He is currently a Research Affiliate in the ESAT-TELEMIC Research Division. His involvement in several industrial research projects, such as with AGFA Healthcare Belgium, resulted in a granted patent and five other filed patents. Upon his return to UniMAP, he resumed his role as a Senior Lecturer, and concurrently served as the Deputy Dean of the university's Research Management and Innovation Center (RMIC), from 2014 to 2017. He researches actively in his areas of interest, such as wearable antennas, arrays, metasurfaces, on-body

communication, electromagnetic safety and absorption, and wireless and radar techniques for healthcare applications. To date, he has led/is leading six internationally and nationally funded projects, besides being involved collaboratively in other projects. He is a member of IET, ACES, and URSI. He was a recipient of the IEEE Antennas and Propagation Society (AP-S) Doctoral Research Award in 2012, the IEEE Microwave Theory and Techniques Society (MTT-S) Graduate Fellowship for Medical Applications in 2013, and the International Union of Radio Science (URSI) Young Scientist Award in 2015. He was also the Second Place Winner of the IEEE Presidents' Change the World Competition and the IEEE MTT-S Video Competition, both in 2013. Two of his (co)authored journals were also awarded the CST University Publication Award in 2012 and 2011. As a project advisor, his supervised students have also won prizes, such as the IEEE MTT-S Undergraduate Scholarship in 2016, the First Place in the Innovate Malaysia Design Competition (Motorola Track) in 2016, and the First Place in the IEEE Malaysia Section Final Year Project Competition (Telecommunication Track) in 2015. He is a Chartered Engineer registered with the U.K. Engineering Council and a Professional Technologist registered with the Malaysia Board of Technologist (MBOT). He also serves in the IEEE MTT-S Education Committee, and the IEEE MTT-S Meetings and Symposia (M&S) Committee.

SALAHUDDIN KHAN is currently an Associate Professor with King Saud University. He is specialized in design, modeling, and simulation which can be extended to various fields of electronics, electromagnetic, and power systems, such as development of algorithms, realization of antenna devices, and power plant secondary systems. The above research lines have produced many research projects and publications. He has also contributed an U.S. patent.

FRANCISCO FALCONE (Senior Member, IEEE) received the degree in telecommunication engineering and the Ph.D. degree in communication engineering from the Universidad Pública de Navarra (UPNA), Spain, in 1999 and 2005, respectively. From February 1999 to April 2000, he was a Microwave Commissioning Engineer with Siemens-Italtel, deploying microwave access systems. From May 2000 to December 2008, he was a Radio Access Engineer with Telefónica Móviles, performing radio network planning and optimization tasks in mobile network deployment. In January 2009, as a Co-Founding Member, he was the Director of Tafco Metawireless, a spin-off company from UPNA, until May 2009. In parallel, he was an Assistant Lecturer with the Electrical and Electronic Engineering Department, UPNA, from February 2003 to May 2009. In June 2009, he became an Associate Professor with the EE Department, being the Department Head, from January 2012 to July 2018. From January 2018 to May 2018, he was a Visiting Professor with the Kuwait College of Science and Technology, Kuwait. He is also affiliated with the Institute for Smart Cities (ISC), UPNA, which hosts around 140 researchers. He is currently acting as the Head of the ICT Section. His research interests include computational electromagnetics applied to the analysis of complex electromagnetic scenarios, with a focus on the analysis, design, and implementation of heterogeneous wireless networks to enable context-aware environments. He has over 500 contributions in indexed international journals, book chapters, and conference contributions. He has been awarded the CST 2003 and CST 2005 Best Paper Award, the Ph.D. Award from the Colegio Oficial de Ingenieros de Telecomunicación (COIT) in 2006, the Doctoral Award UPNA in 2010, the 1st Juan Gomez Peñalver Research Award from the Royal Academy of Engineering of Spain in 2010, the XII Talgo Innovation Award in 2012, the IEEE 2014 Best Paper Award in 2014, the ECSA-3 Best Paper Award in 2016, and the ECSA-4 Best Paper Award in 2017.